Monthly Notices
of the
ROYAL ASTRONOMICAL SOCIETY

MNRAS **447,** 3069–3086 (2015) doi:10.1093/mnras/stu2538

The environments of Ly α blobs – I. Wide-field Ly α imaging of TN J1338−1942, a powerful radio galaxy at $z \simeq 4.1$ associated with a giant Ly α nebula*

Tomoki Saito,[1,2†] Yuichi Matsuda,[3,4] Cedric G. Lacey,[5] Ian Smail,[5] Alvaro Orsi,[6,7] Carlton M. Baugh,[5] Akio K. Inoue,[8] Ichi Tanaka,[9] Toru Yamada,[10] Kouji Ohta,[11] Carlos De Breuck,[12] Tadayuki Kodama[3,4] and Yoshiaki Taniguchi[13]

Affiliations are listed at the end of the paper

Accepted 2014 December 1. Received 2014 December 1; in original form 2014 March 21

ABSTRACT

We exploit wide-field Ly α imaging with *Subaru* to probe the environment around TN J1338−1942, a powerful radio galaxy with a >100 kpc Ly α halo at $z = 4.11$. We used a sample of Ly α emitters (LAEs) down to $\log(L_{\mathrm{Ly}\alpha}[\mathrm{erg\,s^{-1}}]) \sim 42.8$ to measure the galaxy density around TN J1338−1942, compared to a control sample from a blank field taken with the same instrument. We found that TN J1338−1942 resides in a region with a peak overdensity of $\delta_{\mathrm{LAE}} = 2.8 \pm 0.5$ on scales of $8\,h^{-1}$ Mpc (on the sky) and $112\,h^{-1}$ Mpc (line of sight) in comoving coordinates. Adjacent to this overdensity, we found a strong underdensity where virtually no LAEs are detected. We used a semi-analytical model of LAEs derived from the Millennium Simulation to compare our results with theoretical predictions. While the theoretical density distribution is consistent with the blank field, overdense regions such as that around TN J1338−1942 are very rare, with a number density of 6.4×10^{-8} Mpc^{-3} (comoving), corresponding to the densest <0.4 percentile at $z \simeq 4.1$. We also found that the Ly α luminosity function in the TN J1338−1942 field differs from that in the blank field: the number of bright LAEs ($\log(L_{\mathrm{Ly}\alpha}[\mathrm{erg\,s^{-1}}]) \gtrsim 43.3$) is enhanced, while the number of fainter LAEs is relatively suppressed. These results suggest that some powerful radio galaxies associated with Ly α nebulae reside in extreme overdensities on ∼3–6 Mpc scales, where star formation and AGN activity may be enhanced via frequent galaxy mergers or high rates of gas accretion from the surroundings.

Key words: galaxies: evolution – galaxies: formation – galaxies: high-redshift – galaxies: individual: TN J1338−1942.

1 INTRODUCTION

Galaxies are thought to form through accretion of baryonic material (pre-galactic medium, PGM) from their surrounding environment, which provides the cold gas necessary for the star formation process to proceed. The classical picture of this accretion is that the PGM is immediately heated to the virial temperature of the dark haloes (typically $\sim 10^6$ K) to form hot haloes (e.g. Rees & Ostriker 1977). Recent theoretical studies, in contrast, predict that cold gas accretes in the form of cold flows (with temperatures of $\lesssim 10^5$ K) which penetrate the hot haloes surrounding the galaxies and which over cosmic time maintain the star formation activity in galaxies (e.g. Kereš et al. 2005; Dekel et al. 2009). At these low temperatures the gas in the PGM will predominantly cool via Ly α emission. The star formation episodes powered by this accretion in turn provide stellar feedback mechanisms which can then re-heat and eject material in the form of galactic scale outflows (galactic winds; e.g. Veilleux, Cecil & Bland-Hawthorn 2005; Steidel et al. 2010), which subsequently interact with the ambient material in the circumgalactic medium (CGM). Hence, both the accretion and outflows mean that galaxies interact with their surrounding environments, potentially resulting in extended Ly α emission either through cold accretion of the PGM (e.g. Fardal et al. 2001; Dijkstra, Haiman & Spaans 2006; Dijkstra & Loeb 2009; Faucher-Giguére et al. 2010; Goerdt et al. 2010), or from galactic winds ejected into CGM (e.g. Tenorio-Tagle et al. 1999; Taniguchi & Shioya 2000; Mori & Umemura 2006; Dijkstra & Kramer 2012). Such Ly α nebulae may therefore

* Based on data collected at *Subaru* Telescope, which is operated by the National Astronomical Observatory of Japan.

†E-mail: tomoki.saito@ipmu.jp

reflect either the structure of the surrounding material, or gas circulation processes during the formation/evolution of these galaxies (Furlanetto et al. 2005).

The precise mechanisms responsible for forming Ly α nebulae are still unclear. Some Ly α nebulae (e.g. those in the SA 22 protocluster at $z = 3.1$) have been extensively observed, and are thought to be driven by starburst events in massive galaxies forming galactic winds (e.g. Ohyama et al. 2003; Geach et al. 2005, 2009; Wilman et al. 2005; Matsuda et al. 2006; Uchimoto et al. 2008, 2012). Moreover, recent surveys targeting Ly α 'blobs' have also suggested a possible connection between their properties (specifically morphologies) and the environments they reside in (Erb, Bogosavljević & Steidel 2011; Matsuda et al. 2011, 2012). Such an environmental dependence is also qualitatively consistent with the observations of relatively isolated Ly α nebulae, which may point to the possibility that these are accretion driven (Nilsson et al. 2006; Smith & Jarvis 2007; Saito et al. 2008). However, to determine the true significance of environment in the formation of extended Ly α emission haloes, more detailed and systematic observations with sufficient depth and area are essential.

It has been long known that powerful radio galaxies at high redshifts are often associated with large, extended Ly α nebulae (e.g. Chambers, Miley & van Breugel 1990; Röttgering et al. 1995; van Ojik et al. 1996, 1997; Venemans et al. 2007; Villar-Martin et al. 2007). Although these Ly α nebulae appear linked to the radio emission, their properties are similar to the Ly α blobs described above. For example, the large velocity widths exceeding $\sim$1000 km s^{-1} (van Ojik et al. 1997) or absorption across the full extent of the Ly α nebulae (Röttgering et al. 1995; van Ojik et al. 1996) are also seen in the Ly α nebulae in protoclusters (e.g. Wilman et al. 2005; Matsuda et al. 2006). Furthermore, observational studies suggest that large fraction of very luminous Ly α blobs ($\gtrsim 10^{44}$ erg s^{-1}) are likely to be driven by obscured AGNs (e.g. Colbert et al. 2011; Overzier et al. 2013). There appears to be a size dependence of the Ly α nebulae on the size of radio sources (van Ojik et al. 1997), as well as a hint of environmental dependence on the size of the Ly α nebulae (Venemans et al. 2007). Even for those Ly α blobs not directly associated with radio sources, these are sometimes found to be harbouring AGNs (e.g. Basu-Zych & Scharf 2004; Geach et al. 2009). These results suggest that Ly α nebulae are common phenomena reflecting the interaction between massive galaxies and their surrounding environments, regardless of the presence of AGNs. It is thus quite essential to probe the environments of Ly α nebulae with and without radio sources.

We have conducted a systematic, wide-field imaging observations of the environments around known giant Ly α nebulae, as traced by Ly α emitters (LAEs). Here we present the results from the imaging of the first target, the powerful radio galaxy TN J1338−1942 (hereafter TNJ1338) located at $z = 4.11$ (De Breuck et al. 1999). This radio galaxy is known to have a Ly α nebula extending up to $\sim$100 kpc with an asymmetric morphology (Venemans et al. 2002). It has been suggested that this source is associated with a highly overdense region traced by LAEs and Lyman-break galaxies (LBGs), and thus represents an ancestor of present-day clusters, i.e. a *proto*cluster (Venemans et al. 2002, 2007; Miley et al. 2004; Intema et al. 2006; Overzier et al. 2008). Theoretical simulations also suggests that the overdensity associated with TNJ1338 is likely to be an ancestor of a present-day cluster (Chiang, Overzier & Gebhardt 2013). Multiwavelength observations have shown that this source has radio lobes with an extent of $\sim$70 kpc. (De Breuck et al. 2004; Venemans et al. 2007). The extended Ly α nebula around this source has signatures of star formation induced by the radio jet, well outside the host galaxy at radii of $\sim$20 kpc or more (Zirm et al. 2005). Finally, *Chandra* X-ray observations indicate that there is weak extended emission ($\sim$30 kpc) which may arise from inverse-Compton scattering of cosmic microwave background or locally produced far-infrared photons (Smail & Blundell 2013).

Together these observations suggest a number of processes responsible for intense interaction between the central radio galaxy and the surrounding environment. However, due to the lack of the wide-field imaging data, the surrounding environment of this radio galaxy is still not well characterized. The existing LAE survey data cover a small field (two 7 arcmin × 7 arcmin) making it hard to map any overdensity, and there is no matched blank-field observations which means that even the magnitude of the overdensity is uncertain. [Venemans et al. (2007) used the Large-Area Lyman α survey results (Rhoads et al. 2000; Dawson et al. 2004) for the reference, which are taken with the different telescope and instrument, targeting a slightly different redshift]. Accordingly, the relationship between the structure hosting the radio galaxy (and the protocluster) and the wider surrounding environment cannot be probed with the existing data.

The goal of our study is to better quantify the environment of the powerful radio galaxy TNJ1338. To this end, we have obtained wide-field intermediate-band images to identify the LAEs lying at the redshift of the radio galaxy, and so quantify the environment using the LAE number density. The magnitude of the overdensity was determined from comparison with a control sample taken from a blank field, SXDS (Furusawa et al. 2008), at the same redshift and with the same instrumental setup (Saito et al. 2006). This enables us to probe '*on what scale does a significant overdensity exist?*', i.e. the amplitude of the overdensity and the spatial extent of the protocluster. We also compare our observations with predictions derived from combing the Millennium Simulation (Springel et al. 2005) with a semi-analytical model for LAEs (Orsi et al. 2008). This allows us to estimate how rare is the overdensity found around the radio galaxy, and more generally how well the simulation can reproduce such environments. This is the first truly panoramic ($\sim$30 arcmin × 30 arcmin) systematic and quantitative study of the environment of a radio galaxy field at $z \sim 4$.

The rest of this paper is organized as follows. We introduce the data and observational details in Section 2. The procedure to select LAEs from these data is presented in Section 3. In Section 4, we compare the observed density field and luminosity function (LF) of LAEs in the radio galaxy field and the blank field, and then compare the observations to the mock LAEs from the theoretical simulations. Throughout this paper, we use the standard Λ cold dark matter cosmology with $\Omega_{\rm M} = 0.3$, $\Omega_\Lambda = 0.7$, $H_0 = 100h = 70$ km s^{-1} Mpc^{-1}, unless otherwise noted. All the magnitudes are in AB system (Oke 1974; Fukugita, Shimasaku & Ichikawa 1995).

2 THE DATA

2.1 *Subaru* imaging data

We obtained 8.0 h integration through the *IA624* intermediate-band filter centred at $(\alpha, \delta) = (13^{\rm h}38^{\rm m}13\overset{\rm s}{.}9,\ -19^\circ42'29'')$ (J2000.0) on 2008 May 31 and June 01 (UT) with Suprime-Cam (Miyazaki et al. 2002) on the 8.2-m *Subaru* Telescope (Iye et al. 2004), under the proposal ID S08A-072 (PI: Matsuda). For the continuum correction, we obtained archival broad-band imaging in the *B* and *R* bands taken by Intema et al. (2006) from the archive system SMOKA (Baba et al. 2002). The archival i'-band data by the same observers were also obtained to check the contamination using the continuum colour.

Details of the observations are summarized in Table 1. Suprime-Cam has a pixel scale of 0.202 arcsec and a field of view (FoV) of 34 arcmin × 27 arcmin. The intermediate-band filter, *IA624*, has a central wavelength of 6226 Å and bandwidth of 302 Å (full width at half-maximum, FWHM), which corresponds to the redshift range for Ly α at $z = 3.996$–4.245 (*R23 IA filter system*; Hayashino et al. 2000; Taniguchi 2004). Fig. 1 shows the transmission curves of the *IA624*, *B*- and *R*-band filters, and the observed-frame wavelength of the Ly α line at the redshift of TNJ1338 ($z = 4.11$).

The raw data were reduced with SDFRED20080620 (Yagi et al. 2002; Ouchi et al. 2004) and IRAF. We flat-fielded using the median sky image after masking sources. We then subtracted the sky background adopting a mesh size of 64 pixels (13 arcsec) before combining the images. Photometric calibration was obtained from the spectroscopic standard stars, PG1323−086, and PG1708+602 (Massey et al. 1988; Stone 1996). The magnitudes were corrected for Galactic extinction of $E(B - V) = 0.10$ mag (Schlegel, Finkbeiner & Davis 1998). The variation of the extinction in this field is sufficiently small (±0.01 mag from peak to peak) that it does not affect our results.

Table 1. Summary of observations.

Filter	$\lambda_{\rm cent}/\Delta\lambda^a$ (Å/Å)	Exposure time (s)	$m^b_{5\sigma}$ (AB mag)	PSF^c (arcsec)
IA624	6226/302	28800 (1800 × 16)	26.94	0.74
B	4417/807	4800 (1200 × 4)	26.87	0.80
R	6533/1120	5940 (540 × 11)	26.92	0.55
i'	7969/1335	2700 (300 × 9)	26.56	0.64
BR^d	6226/1927	–	26.90	0.74

[a]The central wavelength and FWHM of the filters.
[b]The 5σ limiting magnitudes within a 1.5 arcsec diameter aperture.
[c]The median PSF size (FWHM).
[d]The weighted mean of the *B*- and *R*-band images.

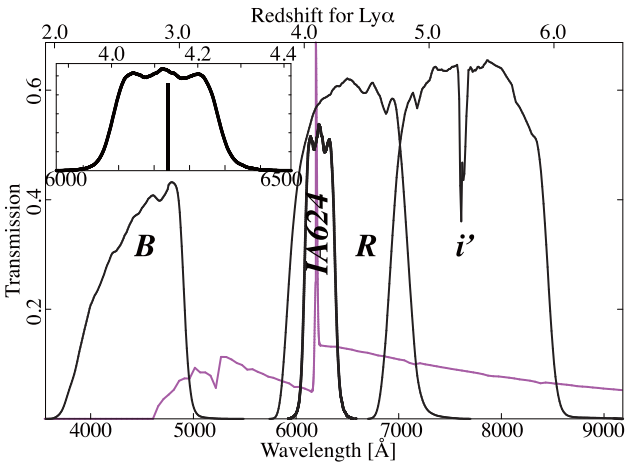

Figure 1. The response curves of our filters. The transmission of the filters is plotted against the wavelength. The lower axis shows the observed wavelength, and the upper axis gives the corresponding redshift for Ly α line. The thick black curve shows the intermediate-band filter (*IA624*) used to select sources with Ly α emission. The two broad-band filters (*B* and *R*) are shown with thin lines. The thick magenta curve shows a model spectrum of a star-forming galaxy created with *GALAXEV* (Bruzual & Charlot 2003) with a Gaussian-profile Ly α emission line, redshifted to $z = 4.1$. The box in the upper left shows a close-up view of the *IA624* filter transmission, together with the redshift of TNJ1338 indicated with a vertical thick bar.

The combined images were aligned and smoothed with Gaussian kernels to match their point spread function (PSF) to a FWHM of 0.74 arcsec. The PSF sizes for some exposures in the *B* band were not as good as the other bands (the median PSF size was 0.8 arcsec), so that we removed these bad-seeing data, using only the four best frames for our analysis. The total size of the field analysed here is 32 arcmin × 24 arcmin after the removal of low-S/N regions near the edges of the images. We also masked out the haloes of the bright stars within the field, resulting in the effective area of 689 arcmin^2 in total. This corresponds to a comoving volume of $1.7 \times 10^5 h^{-3}$ Mpc^3 at $z = 4.1$, covering a radial comoving distance of $112.4\,h^{-1}$ Mpc for sources with Ly α emission lying within the wavelength coverage of the *IA624* filter.

The blank-field data used for the control sample were taken as part of the *Subaru/XMM–Newton* Deep Survey (SXDS) project (Furusawa et al. 2008) and a subsequent intermediate-band survey (Saito et al. 2006). The SXDS field consists of five pointings, centred at $(\alpha, \delta) = (02^{\rm h}18^{\rm m}00\overset{\rm s}{.}0,\ -5^\circ00'00\overset{''}{.}0)$ (J2000). The intermediate-band (including *IA624*) data were taken only in the south field (SXDS-S) centred at $(\alpha, \delta) = (02^{\rm h}18^{\rm m}00\overset{\rm s}{.}0,\ -5^\circ25'00\overset{''}{.}0)$ (J2000). The data were taken with the same instrument on the same telescope, and reduced in the same manner with the same software as our TNJ1338 observations. The PSF was matched to 0.78 (FWHM), and the 5σ limiting magnitudes are 26.60, 27.42 and 27.91 for the *IA624*, *B* and *R*, respectively. After masking out the regions near the edges and bright stars, the total area coverage was 691 arcmin^2, which is almost the same as the TNJ1338 field.

2.2 Mock catalogue of Ly α emitters

In order to compare the observations with the predictions from a cosmological *N*-body simulation (Millennium Simulation; Springel et al. 2005), we exploited a LAE catalogue generated with a semi-analytical model of galaxy formation (GALFORM; Cole et al. 2000; Le Delliou et al. 2005, 2006). This catalogue contains ∼10^6 LAEs with a wide range of luminosity and the Ly α equivalent widths (EWs). The details of this catalogue are described in Orsi et al. (2008). The LAEs in this catalogue were generated by placing model galaxies into dark haloes of masses above the threshold value appropriate for the simulation's mass resolution. The star formation history for each halo was calculated by using a Monte Carlo merger tree. The initial mass function (IMF) was assumed to be top heavy for those stars formed during any starbursts, $\mathrm{d}N/\mathrm{d}\ln(m) \propto m^{-x}$ with $x = 0$, with a standard solar neighbourhood IMF (Kennicut 1983) for those stars which quiescently form in discs, i.e. $x = 0.4$ for $m < 1\,{\rm M}_\odot$ and $x = 1.5$ for $m > 1\,{\rm M}_\odot$. Both IMFs cover the stellar mass range $0.15\ {\rm M}_\odot < m < 125\ {\rm M}_\odot$. The Ly α line luminosity is then calculated from the number of ionizing photons emitted by the corresponding stellar population.

Orsi et al. (2008) compared the properties of model LAEs from their simulation with existing LAE surveys and showed that both the LF and the clustering properties are broadly consistent with the observations. The number density of model LAEs in the luminosity range of ∼$10^{42.5}$–10^{43} erg s^{-1} are slightly higher than observed in the SXDS at $z = 3.1$, but slightly below the SXDS at $z = 5.7$. The difference is up to ∼0.5 dex, so that the accuracy of the model prediction for the LFs should be around ∼±0.5 dex. From this catalogue, we selected LAEs using similar colour constraints to those applied to the observed data, see Section 3 for details of the selection procedure.

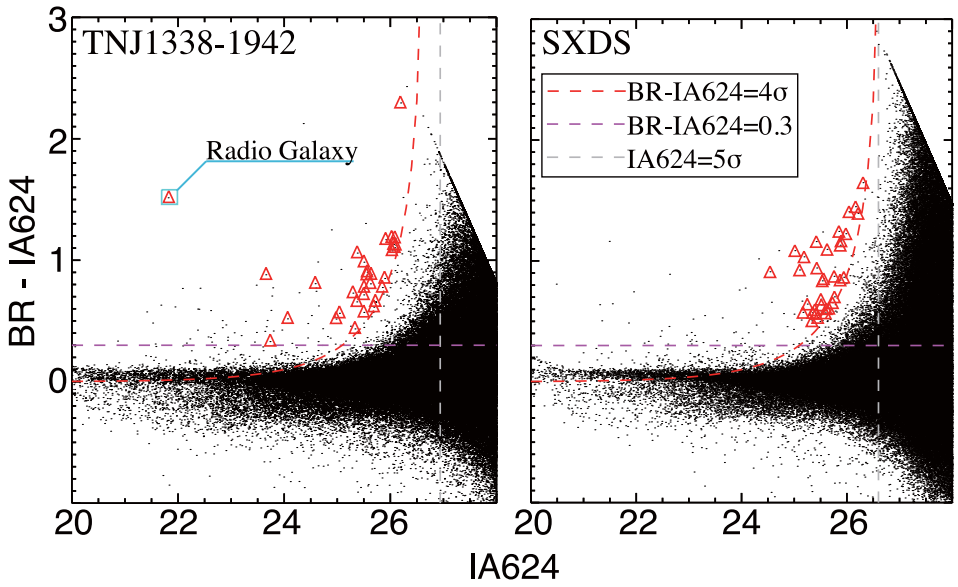

Figure 2. Colour–magnitude diagram. $BR - IA624$ colour as a function of *IA624* magnitude for the TNJ1338 field. Left: The black dots show all the sources, and the red triangles show 4σ-excess LAE candidates. The vertical grey dashed line shows the magnitude cut ($IA624 > 26.6$), the horizontal magenta dashed line indicates the $BR - IA624 > 0.3$ threshold. The red dashed curves show 4σ level of the *IA624* excess. Right: same as the left-hand panel, but for the SXDS blank field.

3 SAMPLE SELECTION

3.1 The TNJ1338 field sample

We used the *IA624* image for detection, and the wavelength-weighted mean of *B* and *R* band images (hereafter *BR*) to determine the continuum level at a rest-frame wavelength of 1216 Å. The *BR* image was generated by combining the two images with

$$BR = \frac{(\lambda_{\mathrm{Ly}\alpha,\mathrm{obs}} - \lambda_B)R + (\lambda_R - \lambda_{\mathrm{Ly}\alpha,\mathrm{obs}})B}{\lambda_R - \lambda_B},$$

where λ_B and λ_R are the central wavelengths of *B* and *R* bands, respectively, and the $\lambda_{\mathrm{Ly}\alpha,\mathrm{obs}}$ is the observed-frame wavelength of the Ly α line at $z = 4.11$. The source detection and photometry were made using the source detection and classification tool, SExtractor (Bertin & Arnouts 1996). The sources detected here have at least five connected pixels above a threshold corresponding to 1.5σ of the sky noise. Using the position of these sources detected in the *IA624* image, photometry was measured in the other bands with the same aperture, after matching the PSF size. We measured photometry for a total of 205 011 sources, after masking.

Based on the photometry catalogue from these three images (*B*, *R*, and *IA624*: *i*′ was not used for the selection since the data is rather shallow), we selected the LAE candidates at $z \simeq 4.1$ by applying the following conditions:

$$20 < IA624 < 26.6 \quad (1)$$

$$BR - IA624 > 0.3 \quad (2)$$

$$B > 27.87, \text{ or, } B - R > 2.17 \quad (3)$$

$$BR - IA624 > (BR - IA624)_{4\sigma}. \quad (4)$$

We first applied the magnitude cut (equation 1) to remove bright foreground contaminants ($IA624 > 20$) and a faint limit to remove false detections ($IA624 > 5\sigma$). Note that the 5σ threshold here is set according to the SXDS data, not the TNJ1338 data, in order to make a fair comparison with the control sample obtained in the SXDS field. The bright threshold, 20 mag, was determined from visual inspection of the sources. This value roughly corresponds to Ly α luminosities corresponding to the brightest high-redshift radio galaxies (e.g. De Breuck et al. 2001; Reuland et al. 2003). Equation (2) selects those sources with Ly α excess in the intermediate-band filter, corresponding to an EW of $\gtrsim$200 Å ($\gtrsim$40 Å in the rest frame). Then we applied a colour selection designed to detect the Lyman break at $z \sim 4$ (equation 3). Finally, equation (4) requires that the *IA624* excess has a significance level of at least 4σ. Note that we used the *BR* matched continuum to estimate the *IA624* excess, although the *B* band should detect almost no flux from $z \sim 4$ sources because the wavelength coverage of the *B* band is mostly below the Lyman limit. However, the distribution of the $R - IA624$ colour is not centred at zero, so that defining *IA624*-excess sources using just the *R*-band continuum level is somewhat unclear. We thus used the *BR* to measure the continuum levels.

Fig. 2 shows the colour–magnitude diagram used for our LAE selection. We need to be aware of the possible contamination due to the noise in the *IA624*-excess measurements: the LAEs should lie well above the scatter around $BR - IA614 = 0$. For some cases, i.e. when the *IA624* is relatively shallow, false detections may dominate sources selected at the 3σ level. We carefully visual inspected all the sources selected here, and we found two sources that are obviously affected by bad regions of the CCD. These sources are in a region affected by a neighbouring bright source. Excluding this, we constructed a sample of 31 LAEs in the TNJ1338 field.

Fig. 3 shows the sky distribution of the LAEs selected above, overlaid on the *IA624* image. The reader should note the apparent 'void' around the north-western part of the field, where relatively few LAEs are detected, and does not seem to be an artefact of the bright stars.

The photometric properties of the sources selected here are summarized in Table 2. We here checked the overlap of our sample with previous studies. We cross-matched the coordinates of our sources with LAEs in the sample of Venemans et al. (2007) and LBGs in Overzier et al. (2008), both observing the same field. We found

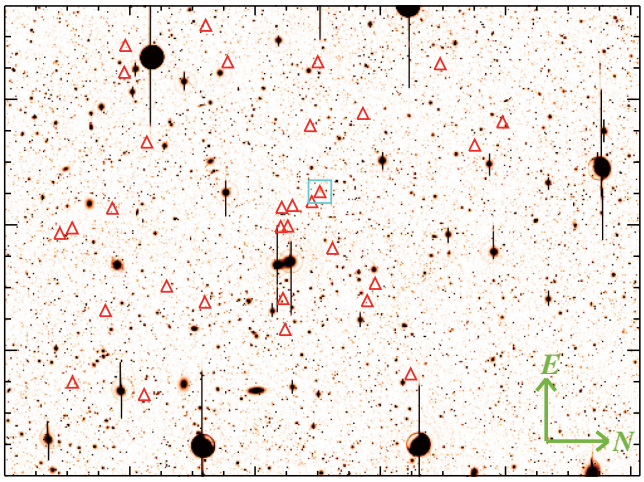

Figure 3. The sky distribution of our LAEs in the TNJ1338 field. The symbols for our photometrically selected LAE sample are the same as Fig. 2, and the position of TNJ1338 is shown with the cyan box. The background is the *IA624* image taken with Suprime-Cam. East is up, and north is to the right.

three sources also included in the previous LAE sample, and four with the LBG sample. Furthermore, when we apply slightly looser colour constraint, $BR - IA624 > 3\sigma$ instead of the equation (4), we have 7 and 11 overlapped sources with the LAE and LBG samples, respectively. This shows that our colour constraints (equations 1–4) are working at least qualitatively well to select LAEs at $z \sim 4$. Since our redshift coverage is ∼5 times wider than that of Venemans et al. (2002, 2007), most of our sources are likely to be located outside Venemans et al.'s coverage. Indeed, only three sources associated with the density peak around the radio galaxy (including the radio galaxy itself) are overlapped with Venemans et al.'s sample. Our sample thus traces the overdense structure larger than ∼33(23 h^{-1}) comoving Mpc along the line of sight. Although most of our sources do not overlap with the other samples of LAEs and LBGs, their UV ($R - i'$) colours are fairly consistent with that expected for $z \sim 4$ galaxies. We computed the mean and the standard deviation of the $R - i'$ colours of our and Venemans et al.'s samples of LAEs, and obtained the colour indices of -0.14 ± 0.49 and 0.19 ± 0.38, respectively. Both of them agree with the $R - i'$ colours of our SXDS control sample within the errors. We then extracted 11 sources with $i' < 26.0$ from our sample ($R - i'$ colours of 0.08 ± 0.4), and found that 10 of them satisfy the LBG selection criteria by Ouchi et al. (2004). The remaining one source has slightly red $R - i'$ colour, but fainter than 1σ level in B band, which is consistent with the Lyman-break feature. In any case, this source lies in relatively

Table 2. List of the photometrically selected LAEs in the TNJ1338 field.

ID	α (J2000)	δ (J2000)	*IA624*	*BR*	B^a	R^a	i'^a	log ($L_{Ly\alpha}$[erg s^{-1}]) ^{b}	Notes
47564	13: 37: 39.77	−19: 51: 57.4	26.06	27.19	28.62	26.91	27.44	43.21	
54822	13: 37: 42.61	−19: 55: 48.4	25.55	26.43	28.60	26.16	26.40	43.34	
58749	13: 37: 44.52	−19: 37: 37.8	24.98	25.49	28.62	25.21	25.36	43.41	
83374	13: 37: 54.64	−19: 44: 22.8	25.50	26.21	28.62	25.92	25.98	43.31	
93306	13: 37: 58.96	−19: 54: 02.5	25.33	25.77	28.62	25.49	24.23	43.21	
97780	13: 38: 00.88	−19: 48: 41.8	26.08	27.19	28.62	26.90	28.31	43.19	
98384	13: 38: 01.22	−19: 39: 58.1	25.50	26.07	28.62	25.78	25.75	43.23	
99860	13: 38: 01.71	−19: 44: 29.6	25.37	26.03	28.44	25.75	25.87	43.33	
106649	13: 38: 04.53	−19: 50: 44.9	25.29	26.02	28.62	25.74	26.10	43.39	
107660	13: 38: 05.17	−19: 39: 32.6	24.06	24.58	27.91	24.30	24.37	43.78	
127592	13: 38: 13.16	−19: 41: 50.0	26.19	28.49	28.62	28.23	26.92	43.29	
135689	13: 38: 16.58	−19: 56: 29.3	25.72	26.38	28.62	26.09	26.11	43.19	
138350	13: 38: 17.81	−19: 55: 49.6	25.04	25.60	28.62	25.32	25.38	43.41	
139312	13: 38: 18.10	−19: 44: 37.0	26.09	27.27	28.62	26.95	27.15	43.21	
139843	13: 38: 18.23	−19: 44: 14.1	25.69	26.30	28.15	26.06	26.59	43.18	
149890	13: 38: 22.31	−19: 53: 40.2	25.50	26.49	28.62	26.23	26.68	43.40	
150274	13: 38: 22.48	−19: 44: 33.7	25.51	26.28	28.62	26.02	25.89	43.33	*d, e*
151277	13: 38: 22.92	−19: 43: 59.3	25.56	26.46	28.62	26.19	26.63	43.35	*e*
153858	13: 38: 23.78	−19: 42: 56.8	26.10	27.23	28.62	26.91	26.98	43.19	*e*
184585	13: 38: 36.63	−19: 34: 11.3	25.62	26.43	28.13	26.17	26.64	43.29	
186397	13: 38: 37.39	−19: 51: 48.8	25.91	27.08	28.62	26.77	26.20	43.28	
194782	13: 38: 41.12	−19: 43: 01.9	23.73	24.06	27.31	23.78	23.65	43.75	*d*
197870	13: 38: 41.91	−19: 32: 41.1	25.38	26.44	28.62	26.16	26.61	43.47	
202840	13: 38: 43.90	−19: 40: 11.5	26.03	27.11	28.62	26.85	27.00	43.21	
225768	13: 38: 53.34	−19: 53: 01.1	23.65	24.53	27.23	24.26	24.27	44.11	
229080	13: 38: 55.18	−19: 36: 02.4	24.58	25.39	28.62	25.12	25.33	43.71	
232509	13: 38: 55.67	−19: 42: 36.9	25.89	26.74	28.62	26.45	26.25	43.20	
232582	13: 38: 55.67	−19: 47: 27.7	25.85	26.62	28.62	26.35	26.64	43.19	
242571	13: 38: 59.45	−19: 52: 57.5	26.03	27.21	28.62	26.98	27.05	43.23	
257624	13: 39: 04.04	−19: 48: 38.6	25.64	26.52	28.62	26.26	26.83	43.31	
155683	13: 38: 26.07	−19: 42: 30.5	21.81	23.33	28.62	23.04	24.05	44.97	*c, d, e*

Notes. (*a*) Broad-band magnitudes are replaced with the 1σ values when the photometry results are below the 1σ level; (*b*) Ly α line luminosities are estimated from the photometry by assuming that they are located at $z = 4.1$; (*c*) radio galaxy; (*d*) also included in the LAE sample of Venemans et al. (2007); (*e*) also included in the LBG sample of Overzier et al. (2008).

less-luminous range of the LF of our sample, and is located in average-density region ($\sim$1.3 $\times$ the average). Even if this source is a foreground contaminant, our result thus does not significantly change. For the sources overlapped with Overzier et al.'s LBG sample, all including the radio galaxy satisfy the colour constraints of LBG, showing that our colour selection is working quite well. We thus concluded that our sample does not contain significant contamination of the foreground sources.

The expected contaminants are [O II]λ3727 emitters at $z \sim 0.7$, and [O III] $\lambda\lambda$4959, 5007 emitters at $z \sim 0.25$. Although our selection corresponds to very large EWs, these contaminants cannot be ruled out simply by their EWs, as there are certain amount of such strong emitters (e.g. Atek et al. 2011; van der Wel et al. 2011). The LFs of such strong emitters are still not studied well, but narrow-band surveys can give a rough estimate of the number density of such populations. Kakazu, Cowie & Hu (2007) pointed out that strong [O III] emitters are the most common among such strong emission line galaxies, and their [O III] LF gives the number density of the sources with EWs of $\log(\mathrm{EW[\AA]}) \gtrsim 2$ to be $\sim 1 \times 10^{-3}\,\mathrm{Mpc}^{-3}$ at $z \sim 0.6$. If we assume that this density is valid for $z \sim 0.25$, the expected number of [O III] λ5007 within our survey volume is around unity, when integrating over the whole luminosity range of our sample. Even if other emitters ([O III] λ4959 and [O II] λ3727) have similar number density, only a few sources would be contained in our sample, which is quite unlikely. To test how the contamination affect our results, we reduced the number of sources by using $BR - IA624 > 5\sigma$ instead of equation (4). This selection excludes one source lying within the high-density region around the radio galaxy, giving the peak overdensity well within the error. This does not make any significant changes in our results, i.e. the density field and the shape of the Ly α LF.

3.2 The control sample in SXDS field

We constructed a control sample of LAEs, using similar imaging data in a blank field (the SXDS-S field, hereafter SXDS). These data were taken with the same instrument and filters as used in the TNJ1338 observations as noted above, and the field is not biased to any known overdense regions at $z \sim 4$. In order to make a fair comparison between the two fields, we defined the colour constraints based on the shallower data of the two, i.e. 5σ limiting magnitudes are assumed to be $IA624 = 26.60$ mag, $R = 26.94$ mag, and $B = 26.87$ mag. We also corrected for the offset of $BR - IA624$ colour distribution for the SXDS field, presumably due to an error in the magnitude zero-point. We then applied a colour term $\Delta(BR - IA624) = 0.15$. This colour term was estimated by fitting a Gaussian function to the colour distribution. We derived the colour offset necessary to force the centre of the colour distribution to zero within the magnitude range $20 < IA624 < 26.60$. Except for applying this colour term, we employed exactly the same colour constraints to select the LAEs in this field. The total number of sources identified is 34. The colour–magnitude diagram for this sample is shown in Fig. 2 together with the TNJ1338 sample.

3.3 The mock LAE sample

In order to make a meaningful comparison between the observations and the simulation, we selected LAEs from the mock LAE catalogue at $z = 4.17$ described in Section 2, which is the output redshift closest to that of TNJ1338. We used the predicted Ly α fluxes and EWs contained in the catalogue, to calculate the colours and magnitudes of the LAEs. Note that the catalogue contains $z = 4.17$ LAEs, while we are going to constrain the observed (apparent) colours of $z \approx 4.11 \pm 0.12$. However, the difference between these two epochs is very small, $\sim$55 Myr, and $z = 4.17$ is well within the coverage of the *IA624* filter. We thus calculated the apparent (observed) colours at $z = 4.11$. This should be a reasonable assumption to compare the simulated LAEs with the observations, since the time-scale of galaxy evolution (e.g. star formation) is much longer than this difference.

We first calculated the absorption of the UV continuum by the intervening inter-galactic medium (IGM), following the formalism of Madau (1995). Here the UV continuum was assumed to be flat in terms of flux density per unit frequency bin, $f_\nu = \mathrm{Const}$. The flux density was obtained by dividing the Ly α flux by EW (observed), $f_\lambda = F(\mathrm{Ly}\alpha)/W_{\mathrm{obs}}$. Then the IGM absorption was calculated by assuming the redshift of $z = 4.11$ to obtain the continuum component of the spectrum expected at the redshift of the radio galaxy. The UV continuum contribution to the photometry was calculated by convolving the flat-continuum spectrum with the filter response curves. The IGM absorption on the Ly α line is included in the escape fraction, f_{esc} used in generating the mock catalogue of LAEs (see Orsi et al. 2008). Then sufficiently narrow-line profiles (i.e. narrower than the *IA624* passband) were convolved with the filter response curves, and the line contribution to the photometry was obtained.

Adding the contributions from both the Ly α line and the UV continuum, we calculated the *R*- and *IA624*-band magnitudes to apply the colour constraints. Since our calculation gives exactly the same continuum colour for all sources, we did not apply the constraints on the $B - R$ colour. This does not affect our results because the mock LAE catalogue does not contain any foreground contamination. Furthermore, the *B*-band magnitude cannot be predicted from our calculation with sufficient reliability, because we are assuming a very simple IGM absorption model. Due to the Lyman-break feature and the Gunn–Peterson trough, the high-z sources are expected to be fainter in *B* than in the *R* band. We indeed required in equation (3) that $B - R > 2.17$, which leads to be $\gtrsim$0.15 fainter *BR* magnitudes than the *R*. In order to put the same colour and magnitude constraints as for the observed samples, we then put the offset of +0.15 mag on the *R*-band magnitudes when computing the *IA624* excess, instead of using *BR* magnitudes. This gives the following criteria for selecting the LAEs:

$$20 < IA624 < 26.6 \tag{5}$$

$$R - IA624 > 0.15 \tag{6}$$

$$R - IA624 > (BR - IA624)_{4\sigma}. \tag{7}$$

For the significance level of the *IA624* excess, $(BR - IA624)_{4\sigma}$, the same value as in equation (4) was used to match the observed sample. For the comparison with the observed samples, we applied the magnitude cut of $IA624 < 26.6$ for equation (5), and the observed *IA624*-excess threshold of $(BR - IA624)_{4\sigma}$. In total we select 59 639 model LAE sources in a comoving volume corresponding to $(500\,h^{-1}\,\mathrm{Mpc})^3$.

4 RESULTS AND DISCUSSION

4.1 Density field

4.1.1 The high-density region around the radio galaxy

We quantified the difference between the TNJ1338 and SXDS fields by constructing their LAE surface density maps. We smoothed the

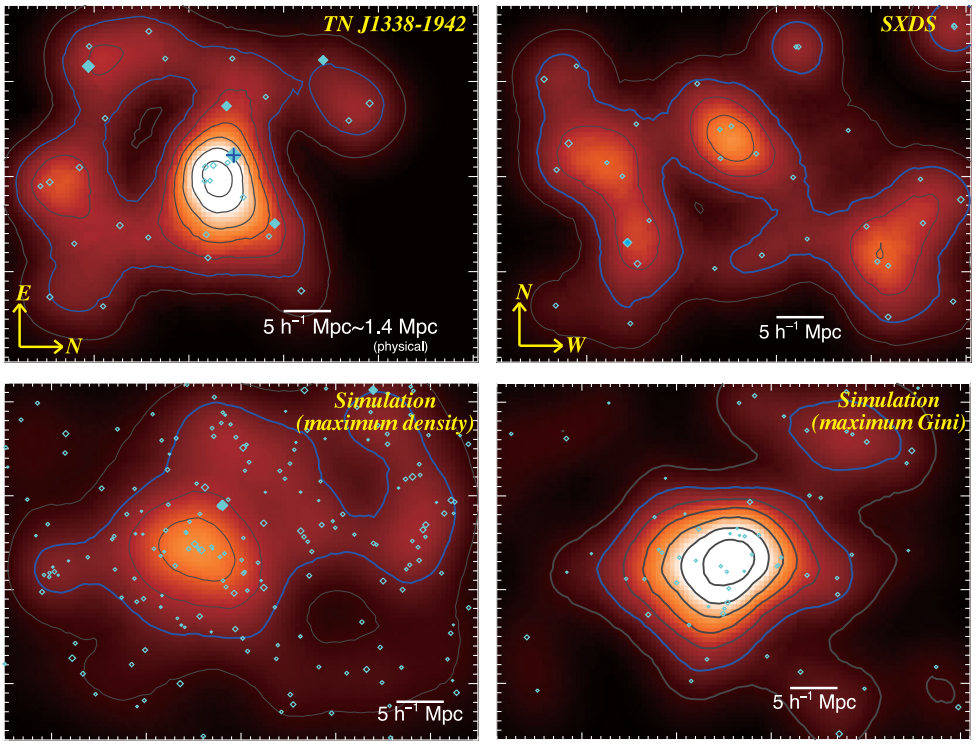

Figure 4. A comparison of the density field of LAEs. The top panels are the observed density map of the TNJ1338 field (left), and the SXDS field (right). The position of the radio galaxy TNJ1338 is shown with the blue cross mark near the density peak. The bottom panels are simulated density maps generated from the mock LAE catalogue using the same selection as those applied to the observed data, showing the same FoV centred on density peaks which are higher than that measured at the position of the radio galaxy: the field around the maximum density peak (left) and the field with the highest Gini coefficient (right). Each panel shows the $50 \times 38\,h^{-2}$ Mpc^2 (comoving) field. The contour interval is 0.5 times the average density over the same FoV, with a lowest contour of 0.5 ($\delta_{\rm LAE} = -0.5, 0.0, 0.5, 1.0, \ldots$). The thick blue contour traces the average density over the field ($\delta_{\rm LAE} = 0.0$). The cyan diamonds mark the positions of LAEs, and the sizes of these symbols represent the Ly α luminosities. The sources with $\log(L_{{\rm Ly}\alpha}[\,{\rm erg\,s^{-1}}]) \gtrsim 43.6$ are marked with filled symbols.

spatial distribution of the LAEs with a Gaussian kernel with a radius (half-width at half-maximum, HWHM) of $4\,h^{-1}$ Mpc (projected comoving distance at $z = 4.1$, corresponding to the physical distance of 1.1 Mpc), and counted the number of LAEs within the same radius at each grid point, with a grid spacing of $0.5\,h^{-1}$ Mpc. Then the surface density was obtained by dividing the number by the area of the Gaussian aperture with the HWHM of $4\,h^{-1}$ Mpc. In deriving the average surface density, the areas within $5\,h^{-1}$ Mpc of the edge of the FoV were flagged to avoid underestimating the surface density near the field edges. The kernel size was chosen based on the typical separation between the sources. We measured the distance to the nearest source for each LAE in our sample, and chose the smoothing kernel size to include ~68 per cent of the whole sample. We confirmed that different sizes of the smoothing kernel also give a similar density distribution. Note that the radio galaxy itself was excluded in creating the density map, since we are aiming to investigate the surroundings of the radio galaxy.

The density maps we obtained are shown in the Fig. 4. We can clearly see that the region around the radio galaxy is strongly overdense, and equivalently strong density peaks are not seen in the SXDS field. The density peak in the TNJ1338 field is ≈4 times the density averaged over the field, while the maximum peak in the SXDS field is only $1 + \delta_{\rm LAE} = 2.36$. We then estimated the uncertainty of the density with this smoothing scale by computing the standard deviation of the density map of the SXDS field, determining the 1σ dispersion in $\delta_{\rm LAE}$ as 0.47. The radio galaxy TNJ1338 is located in the densest region in the field, with $1 + \delta_{\rm LAE} = 2.91$ at its position. The peak density is $1 + \delta_{\rm LAE} = 3.80$, located $2.8\,h^{-1}$ Mpc offset from the position of the radio galaxy. This overdensity can be traced on ~10–20 h^{-1} Mpc scales around the radio galaxy (~3–6 Mpc in physical). Outside this region, in contrast, the density appears to drop quite rapidly: on the northwestern side of the field there is a strongly underdense region just $\sim 20\,h^{-1}$ Mpc from the density peak. Such a strong variation in the density of LAEs is not seen in the SXDS field. Although the overdensity of the TNJ1338 field had previously been suggested by Venemans et al. (2002), their FoV was much smaller than ours, and they were forced to estimate the overdensity (a factor of ~3–5) through comparison to a separate field survey at a similar redshift (Rhoads et al. 2000). With our wide-field imaging of this field, we have not only confirmed the overdensity by comparing with an identically observed control field, but have also determined the spatial scale and structure of the overdense region.

The difference between the TNJ1338 field and SXDS control field becomes clearer when comparing their density histograms, as shown in Fig. 5. In the SXDS field the distribution is concentrated near the average value, while the TNJ1338 field shows a much broader distribution extending towards both high and low densities. In order to quantify the difference between the distributions in these two fields, we first compared the 10th and 90th percentiles for the density maps of the two fields. The upper panel of Fig. 5 shows the cumulative density distributions for the two fields, together with the percentiles. The statistics of the two fields are also summarized in Table 3. The TNJ1338 field has a wider density distribution compared with the SXDS field, especially at the lower density end. The 10th percentile for the TNJ1338 field is $1 + \delta_{\rm LAE} = 0.05$, which

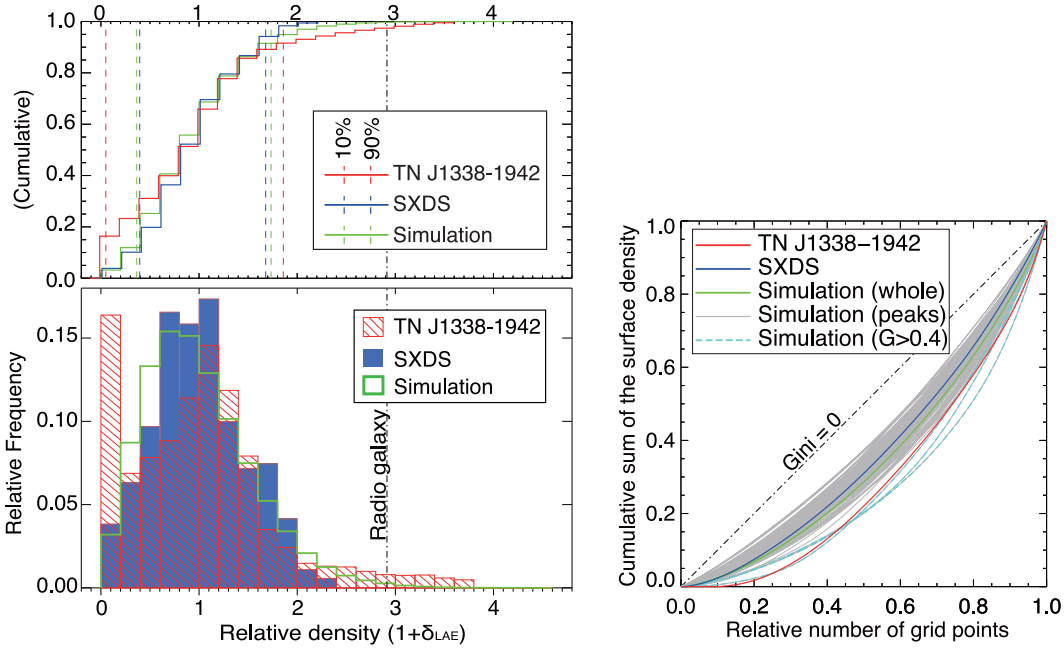

Figure 5. The statistics for the LAE surface density distribution. Left: a comparison of the LAE surface density distributions for the two fields. The red hatched and the blue filled histograms show the density distribution for the TNJ1338 field and the SXDS control field, respectively. Overplotted with the thick green line is the histogram for the simulated density map obtained from the mock LAE sample. The vertical black dot–dashed line shows the density calculated at the position of the radio galaxy. The cumulative distributions are shown in the top panel. The red, blue and green lines denote the TNJ1338, the SXDS and the simulated map, respectively. The 10th and 90th percentiles are shown with the vertical dashed lines with the corresponding colours. We can see that the density distribution in the TNJ1338 field is much wider than that in the SXDS. The simulated density distribution is closer to the SXDS than to the TNJ1338 field. Right: Lorentz curves for the density distribution. The normalized cumulative distribution is plotted against the normalized number of the grid points. The red, blue and green curves show the TNJ1338, the SXDS and the simulated map, respectively. Again the simulated distribution is closer to that of the SXDS field rather than the TNJ1338 field. The grey curves denote the 94 fields centred at the high-density peaks found in Section 4.3.1, of which 21 have *G*s higher than that of the whole simulated map. The three fields with the largest *G*s among the 94 ($G \geq 0.4$) are shown with the cyan dashed curves. The TNJ1338 field has much higher *G* than most of the high-density fields found in the simulation: only two out of 94 have higher *G*s compared with the TNJ1338 field.

Table 3. Statistics of the observed density field.

Field	Mean[a] (h^2 Mpc^{-2})	Peak[b]	Percentiles[c] 10	50	90	G[d]
TNJ1338	0.0201	3.80 (3.73)	0.05	0.98	1.86	0.402
SXDS	0.0204	2.36	0.40	0.97	1.68	0.268

[a]Mean surface density over the field in comoving scale.
[b]Peak normalized surface density ($1 + \delta_{\rm LAE}$). The value normalized with the average of SXDS field is shown in the parenthesis.
[c]In units of the normalized density ($1 + \delta_{\rm LAE}$).
[d]Gini coefficient of the density distribution.

is eight times lower than that of the SXDS field. The ratios of the two (10th and 90th) percentiles, i.e. the dynamic range of the density, for the TNJ1338 and the SXDS fields are 37 and 4.2, respectively. The TNJ1338 field has thus nearly an order of magnitude higher range in galaxy density than that seen in the SXDS field. The difference becomes even more obvious when we look into the highest and the lowest density bins: e.g. $1 + \delta_{\rm LAE} < 0.01$ corresponds to the lowest 9.5 per cent of density cells in the TNJ1338 field, while in the SXDS field only ∼0.2 per cent of the total grid points have such a low density.

A useful statistic to quantify the range of the density distribution is the Gini coefficient of the density field. The Gini coefficient, *G*, measures how uniformly LAEs are distributed within the field, and takes a value of $0 < G < 1$. The *G* value corresponds to the area surrounded by the two Lorentz curves that correspond to the given distribution and $G = 0$ (shown in Fig. 5). If all the LAEs are concentrated within one grid point, then *G* is unity. If the LAEs are distributed uniformly over the field, then *G* is zero. The Lorentz plot shown in Fig. 5 clearly shows that the TNJ1338 field has much higher *G* than the SXDS blank field, and the blank field agrees well with the simulation. The Gini coefficients of the density maps were calculated to be 0.402 (0.268) for the TNJ1338 (SXDS) field. This difference shows that the LAEs are more concentrated into high-density regions (especially into the high-density peak around the radio galaxy) in the TNJ1338 field, compared with the SXDS field. Together these statistics suggest that the galaxy density in the TNJ1338 field traced with LAEs is highly concentrated within the high-density region near the radio galaxy, but that there are also unusually low-density regions in the field where the number of LAEs is highly suppressed. This is quite different from the density field in the SXDS field.

4.1.2 *Density contrast within the TNJ1338 field*

Although the TNJ1338 field has a very large dynamic range in LAE density, the average density of this field over the FoV of Suprime-Cam is still almost the same as that of the SXDS field. The average surface density of LAEs for these two fields is 0.0201 h^2 Mpc^{-2} and 0.0204 h^2 Mpc^{-2} for the TNJ1338 and the SXDS field, respectively. This suggests that the density traced by LAEs is almost uniform (within ∼2 per cent) at ∼50 h^{-1} Mpc scales, when the density field is averaged over ∼112 h^{-1} Mpc along the line of sight (both in

comoving scale). Even with this smoothing, there is a significant overdensity around the radio galaxy, and a similarly significant underdense region just adjacent to it. This 'void' region next to the high-density region corresponds to the peak of the density distribution near zero in the histogram (Fig. 5). The shape of this distribution is quite different from that for the SXDS field.

Due to the limited number of sources, ∼30 in each field, it is not clear whether the underdense region is truly a void. However, the detectable (i.e. bright and large-EW) LAEs were not found in this region, especially in the northwestern quarter of the field. This appears to be a real effect since there are no bright stars in this region that would significantly affect the detection and photometry, as seen in the Fig. 3. Such a large underdense region is not seen in the SXDS field, again showing that this radio galaxy field has an unusually high-density contrast. The real density contrast in this radio galaxy field is possibly higher than estimated, since we are smoothing the spatial distribution along the line of sight as a result of the relatively wide redshift coverage of the *IA624* filter. Although the apparent contrast would be enhanced due to the redshift-space distortion if the high-density region is actively accreting the material, such an effect is thought to be small because of the wide redshift coverage.

Such a large density contrast within a single field suggests that the high-density region around the radio galaxy is attracting material from well within the scale of the Suprime-Cam FoV ($38 \times 50\,h^{-2}$ comoving Mpc^2 on the sky, when the edges are flagged out), because the average density is almost the same as the blank field. If LAEs are tracing the matter distribution, then the surrounding dark haloes within this scale should have been merging into this overdensity. Since we do not have spectroscopic data for all the sources, we cannot draw any clear conclusions on the true spatial structure of the overdensity based solely on our current observations: it is not clear whether the density peak represents a single extremely overdense halo, or a less overdense filamentary structure elongated towards the line of sight (the latter case includes the case that two or more clumps are aligned along the line of sight). Nevertheless, the density contrast must have grown to a level high enough to form such a high-density peak and a large void region. Even for the latter case, the high-density filament must have accreted material from its surroundings and grown to a sufficient length to evacuate the void region. Hence in both cases, the spatial extent of the high-density region should be fairly compact (or the filament should be narrow), as the TNJ1338 field shows a large void fraction and the high-density region extends only up to $\sim 20\,h^{-1}$ comoving Mpc (∼6 Mpc in physical units) scales.

This requires that matter is concentrated into a high-density region of $\sim$10–20 h^{-1} comoving Mpc size (∼3–6 physical Mpc), well before the observed epoch of $z \sim 4.1$. Such a concentration should affect the star formation and AGN activity of galaxies within the overdensity, in the form of, e.g. frequent galaxy mergers. This may therefore lead to an excess of massive galaxies harbouring active star formation and/or AGN activity. The corresponding high matter concentration will also lead to a higher rate of gas accretion from the surrounding environment, again resulting in the enhancement of star formation and AGN activity.

4.2 Luminosity function

4.2.1 Comparison with the blank field

As described above, we have found that the TNJ1338 field has a high-density region around the radio galaxy, and a strong density contrast between this and the large void region just adjacent to the peak. To investigate the variation in the LAE LF Fig. 6 compares the Ly α LFs of the LAEs in the TNJ1338 and the SXDS fields. We can see that the faint-end slope of the LF in the TNJ1338 field is significantly shallower than the SXDS, below a Ly α luminosity of $\log(L_{\mathrm{Ly}\alpha}[\mathrm{erg\,s^{-1}}]) \sim 43.3$. On the other hand, the LF in the SXDS field increases nearly monotonically down to our completeness limit, $\log L_{\mathrm{Ly}\alpha} \sim 42.8$, as the L^* is still slightly below the faintest data point (Ouchi et al. 2008, hereafter O08). In the TNJ1338 field, a similar trend can be seen in the LF for LAEs within the overdense region. We plotted the LF of the subsample of LAEs lying within regions with densities higher than the average of the whole Suprime-Cam field ($\delta_{\mathrm{LAE}} \geq 0$). The faint end of this LF agrees with that of the SXDS field, but has higher values than in the SXDS by up to an order of magnitude. Note that the radio galaxy itself ($\log L_{\mathrm{Ly}\alpha} \approx 45.0$) is excluded in the LFs plotted here. The LAE population in the TNJ1338 field is thus thought to be highly biased to bright sources, and the fraction of faint LAEs is reduced in this field. The shape of the bright end may suggest that our LAE sample consists of two different components, e.g. star-forming galaxies dominating the faint end, and AGN hosts dominating the bright end. This should be real even if the bright end contains foreground contamination. As mentioned in Section 3, the LF of foreground sources suggests that the expected number of [O II] emitter is around unity, even when integrated down to our completeness limit. The number of LAEs with $\log(L_{\mathrm{Ly}\alpha}) \gtrsim 43.6$ is four in the TNJ1338 field (excluding the radio galaxy), while that in the SXDS field is only one. It is unlikely that more than one such bright foreground sources are included in our

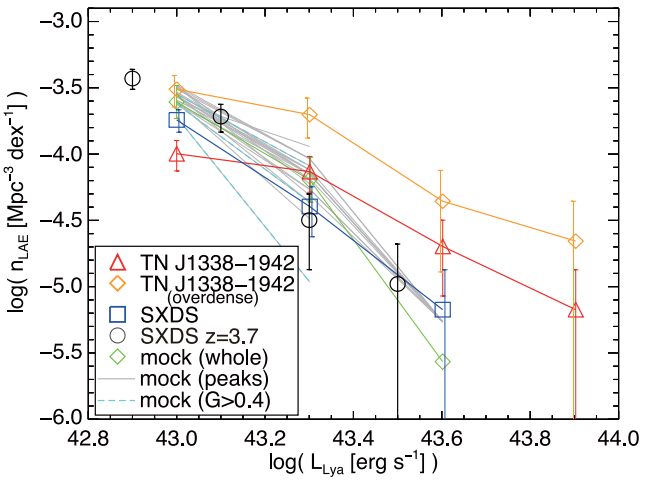

Figure 6. The Ly α LF of the observed samples of LAEs. The red triangles show the LF of the total LAE sample in the TNJ1338 field. The subsample lying within the overdense regions (higher than the average of the field) is shown with the orange diamonds. The blue squares denote the SXDS control sample. The black circles shows the LF of $z \simeq 3.7$ LAEs in the SXDS field, taken with a narrow-band filter (Ouchi et al. 2008). The green diamonds show the LF of the mock LAE catalogue by Orsi et al. (2008), and the grey lines show the LF derived from the subsample of the mock LAEs residing within the Suprime-Cam-sized fields centred at the positions of 21 high-density peaks with high Gs. The LFs of the three highest G peaks among these 21 are marked with the cyan dashed lines. The radio galaxy TNJ1338 is omitted to show the luminosity range of the normal LAEs. Note that the data points are slightly shifted to improve the visibility. We can see that the number of bright LAEs is enhanced in the radio galaxy field, and the fraction of the faint LAEs is reduced. The LF within the overdense regions has almost the same shape as that within the whole field, but the absolute number density agrees with that in the SXDS at a luminosity of $\log(L_{\mathrm{Ly}\alpha}[\mathrm{erg\,s^{-1}}]) \sim 43.0$.

sample, and thus the enhancement of the bright LAEs is thought to be real.

We have also compared the SXDS control sample with a narrow-band-selected LAE sample at a similar redshift in the same field, to check the reliability of our control sample. The LF of the SXDS control sample agrees quite well with the LF of the narrow-band-selected LAE sample at $z \simeq 3.7$ (O08), down to the completeness limit ($\log(L_{\mathrm{Ly}\alpha}) \sim 42.8$). Since the bandpass of the *IA624* filter is several times larger than the *NB570* narrow-band filter, the survey volume is comparable to that of O08, even with only one FoV of Suprime-Cam. This reduces the field-to-field variance, as the density fluctuations are smoothed out along the line of sight. Thus, we confirmed that our SXDS sample is a valid control sample in terms of Ly α LF, representing the typical number density of LAEs at $z \sim 4$. The LF in the TNJ1338 field, on the other hand, lies beyond the variance expected from the results of O08. At the brightest end of the LF, $\log L_{\mathrm{Ly}\alpha} \gtrsim 43.9$, we did not find any sources in the SXDS field, while we still found sources in the TNJ1338 field even when we exclude the radio galaxy itself. Such bright sources are almost never seen in blank-field surveys for LAEs at similar redshifts (Dawson et al. 2007; O08).

These results reinforce the idea that the TNJ1338 field is unusual, not only in terms of the overdensity of LAEs, but also the Ly α LF. Since our *IA624* data are deeper in the TNJ1338 field than in the SXDS field, this should not be due to the difference in the completeness. We mentioned in Section 4.1.2 that the density contrast in this field implies that the high-density region is accreting material from well within $\sim 50\,h^{-1}$ Mpc scale. At this scale, such accumulation of the material is likely to be affecting the star formation and/or AGN activity in galaxies and hence galaxy formation and evolution, leading to the enhancement of the bright end of the Ly α LF. The bright end of the Ly α LF is thought to be dominated by AGN hosts and/or actively star-forming galaxies, so that the formation of such 'active' galaxies is likely to be enhanced in the TNJ1338 field.

4.2.2 *Implications for galaxy formation*

The high-density region around the radio galaxy is so unusual that it faces the large void region. The material originally in the void region must have moved into the surroundings by the epoch of $z \simeq 4.1$, and among the 'surroundings', the high-density region around the radio galaxy is the most prominent peak. This suggests that some large fraction of the material originally in the void region may have travelled to the vicinity of the radio galaxy. Then, how well can this scenario account for such a high-density contrast as we found? We made a rough estimate to test this scenario. The separation between the density peak and the void region is $15\text{-}20\,h^{-1}$ Mpc in comoving scale, which corresponds to $\sim$4-6 Mpc in physical scale at $z = 4.1$. If the material travelled this distance within a Hubble time at this redshift, the velocity is required to be $\sim 4\text{-}6 \times 10^2\,\mathrm{km\,s^{-1}}$. This is although a very naive estimate, as is just the velocity required to travel linearly from the centre of the void to the density peak. In terms of the void evolution, the required velocity is slightly smaller: the apparent radius of the completely empty void is $r \sim 2-3$ Mpc, leading to the peculiar velocity at the edge of the void is around $\frac{1}{3}H(t)r \sim 2\text{-}3 \times 10^2\,\mathrm{km\,s^{-1}}$. These values are well below the typical velocity dispersion of the present-day (virialized) galaxy clusters. Although the required peculiar velocity may be larger than this because the distance assumed here is just the projected distance, the high-density region can be to some extent responsible for accreting the material initially in the void region.

It is however quite unlikely that all of the material initially in the large void had been simply accreted on to the high-density region by the epoch of $z \simeq 4.1$. The material should in principle flow out in all directions from the centre, so that the single overdense region cannot be fully responsible for the formation of the void. The simplest interpretation for the observed (apparent) density contrast is that the initial density fluctuation is quite large, and the contrast had existed since an epoch well before $z \simeq 4.1$. Another interpretation is the enhancement of star formation activity within overdense regions (e.g. Steidel et al. 2005; Koyama et al. 2013), leading to the enhancement of actively star-forming galaxies possibly dominating the bright end of the LF. This may result in a drastic enhancement of the galaxy bias for bright sources. The excess of extreme starbursts within protoclusters found in some observational studies (e.g. Blain et al. 2004; Capak et al. 2011; Ivison et al. 2013) is consistent with this idea. Because of the lack of spectroscopic data, we cannot discriminate between star formation and AGN activities. It is thus also possible that AGNs are dominating the bright end of the LF, which is highly enhanced in the radio galaxy field. Such an enhancement of AGN activity in overdense environments has been found observationally in some cases (e.g. Pentericci et al. 2002; Croft et al. 2005; Lehmer et al. 2009; Digby-North et al. 2010). Since our samples are relatively biased to bright LAEs, such effects will enhance the apparent density contrast.

The difference between the LFs in the two fields depends strongly on the luminosity. When we examine the LF for the overdense regions in the TNJ1338 field, the difference for the luminosity range $\log L_{\mathrm{Ly}\alpha} \gtrsim 43.3$ (corresponding to the brightest two data points for the SXDS field) is about an order of magnitude. This luminosity range contains 15 sources for the TNJ1338 field (all in the overdense regions), while only 7 lie within this range in the SXDS field. On the other hand, both LFs agree with each other within their error bars (factor of $\sim$1.6) at $\log L_{\mathrm{Ly}\alpha} \sim 43.0$. The difference in the faintest data point roughly corresponds to the difference in the total number density for the two fields (the whole SXDS field and the overdense region of the TNJ1338 field). We estimated that the mean density within the overdense regions shown here is $\sim$1.6 times the average of the SXDS, corresponding to $\delta_{\mathrm{LAE}} \sim 0.6$. Since the LF for the overdense regions in TNJ1338 exceeds the LF in the SXDS field by an order of magnitude on the bright end, the overdensity of the bright ($\log L_{\mathrm{Ly}\alpha} \sim 43.6$) LAEs is $\delta_{\mathrm{LAE}} \sim 5$ or so. This means that, if we assume the galaxy bias for LAEs at $\log L_{\mathrm{Ly}\alpha} \sim 43$ to be $b \sim 2.4$–4 (e.g. Ouchi et al. 2005, 2010; Kovač et al. 2007; Chiang et al. 2013), and the faint LAEs are correctly tracing the matter density of this field, the bias for brighter LAEs must be $b \sim 20$–40.

Such a strong luminosity dependence of the bias seems to be rather different from the prediction of the model of Orsi et al. (2008), which predicted only a modest dependence of bias on LAE luminosity. This may suggest that the bright end of the LF is dominated by populations other than the normal star-forming galaxies included in that model, such as hosts of AGN or AGN-induced star formation activities. However, it is still not clear if this result is truly against the prediction. The bias measurement of Orsi et al. (2008) is based on clustering on large scale, so that the results are different from ours. Furthermore, their fig. 6 shows large uncertainty on the bias at the very bright end of the model LAEs, $\log L_{\mathrm{Ly}\alpha} \sim 43$, and it is still possible that the bias of such bright LAEs depends strongly on the luminosity, even for the model LAEs. Orsi et al. (2008) did not present predictions of the clustering bias for LAEs brighter than $\log L_{\mathrm{Ly}\alpha} \sim 43.0$, because their simulation did not contain enough such LAEs for an accurate measurement on large scales.

We here showed only the simplest estimate of the galaxy bias, since we are heavily affected by small number statistics due to having only ∼30 LAEs in each field. We cannot probe the scale dependence of the galaxy bias either: the bias estimated above is on a comoving scale $\sim 20-30\,h^{-1}$ Mpc, which corresponds to the area inside the contour of average density in Fig. 4. Note again that this is smoothed over $\sim 112\,h^{-1}$ comoving Mpc along the line of sight. We can then qualitatively say that there apparently exists a large density contrast within $\sim 50\,h^{-1}$ comoving Mpc scale around the radio galaxy TNJ1338, apparently enhanced to some extent by highly biased nature of the bright LAEs including AGN hosts.

4.3 Comparison with the mock catalogue

4.3.1 Density field of the whole simulated map

We compared the density field shown in Section 4.1 with the mock LAE sample, and evaluated the density distributions of the TNJ1338 field, as well as the control field. The simulated density maps were obtained by applying the same analyses to the mock LAE catalogue described in Section 3.3. We used the same smoothing radius, $4\,h^{-1}$ comoving Mpc, in this process. The simulation covers a comoving volume of $(500\,h^{-1}\,\mathrm{Mpc})^3$. Our *IA624* filter covers a radial comoving distance of $\approx 112\,h^{-1}$ Mpc, so that we can obtain four independent slices perpendicular to the line of sight to create mock sky distributions of LAEs. After selecting the LAEs with similar colour constraints to the observed samples, we extracted the LAEs within a slice of thickness (distance along z-axis of the simulation box) of $112.4\,h^{-1}$ Mpc, and projected them on to the xy plane. In this process, we took account of the effect of redshift-space distortions. The redshift-space coordinates were computed by taking the z-axis as the line-of-sight direction, adopting the distant observer approximation. We then smoothed the spatial distribution of LAEs projected on the xy plane, and counted the LAEs within a smoothing radius centred at each grid point. The simulated LAE density map covers ∼100 times larger area for each slice than a single pointing of the Suprime-Cam, and thus ∼400 times larger volume for the four slices together.

We first used this whole simulated map to compare the density distribution with the observational data. Fig. 5 shows the density histogram of the whole simulated map, overlaid on the observed density histograms. We see that the density distribution of the simulated map is at least qualitatively consistent with that of the SXDS field. The distribution is close to Gaussian with a slightly longer tail towards the high density, peaked around the mean density. The peak amplitude and the width of the peak both look close to that of the control sample. At higher density, on the other hand, the simulated map has a longer, more extended tail than that of the control sample. This looks still consistent with the control sample, because the field coverage of the observational data is much smaller than the simulation. However, the high-density tail seen in the TNJ1338 field is larger than that in the whole simulated map.

Statistical tests also support this difference between the SXDS and TNJ1338 fields, in terms of the comparison with the simulated map. The 10th and 90th percentiles of the density in the simulated map are 0.37 and 1.73, respectively, and the ratio between the two percentiles is 4.7, which is closer to that in the SXDS (4.2) than in the TNJ1338 field (37.3): see Fig. 5 left and Table 3. We also calculated the Gini coefficient of the simulated density map, $G = 0.302$, and compared with the observed distributions in the two fields (Fig. 5 right). The dynamic range of the LAE density for the simulated map is thus in between those of the two observed fields, and closer to the SXDS field than the TNJ1338 field. We then assume that the SXDS field has a typical density distribution of LAEs at $z \sim 4$, and we can evaluate how rare the high-density region seen in the TNJ1338 field is. The density measured at the position of the radio galaxy is $1 + \delta_{\mathrm{LAE}} = 2.91$. Such high-density regions are quite rare in the simulated map, corresponding to the densest 0.07 percentile of the whole volume, while the same overdensity corresponds to the 2.9 percentile of our survey volume in the TNJ1338 field.

It is also important to check the size of field-to-field variations within the simulation volume. To do this, we first obtained density maps centred at random positions. We selected 100 positions in each of the four slices within the central $440 \times 440\,h^{-2}\,\mathrm{Mpc}^2$, and made density maps within a FoV of Suprime-Cam centred at these 400 points. Then we calculated the standard deviation for each bin of the density distribution using the 400 maps. Fig. 7 shows that the observed density distribution, especially the density contrast within a single field, is very different from that for the simulated map as a whole. The volume fraction within the medium- to high-density ($1 + \delta_{\mathrm{LAE}} \sim$ 1–3) bins in the TNJ1338 field agrees with that obtained from the whole simulation volume, at 1σ level. On the other hand, the relative frequencies for the lowest and the highest density bins do not agree with those for the simulated map. This also suggests that such extreme overdensities/underdensities as we found observationally are quite rare in the simulation: the random sampling in the simulated map is unlikely to reproduce the unusual density distribution observed in our field. In fact, we found only 94 density peaks higher than that measured at the radio galaxy position, over the whole simulated map. Among the fields centred at the 94 peaks, only 21 have Gs higher than that of the whole simulated map (see Section 4.3.2). Since the TNJ1338 field has higher G than the whole simulation (and the SXDS field), the number density of TNJ1338-like field is thought to be close to that of such high-G fields. The number density is thus comparable to that of Coma-type protoclusters identified in the same simulation (58 protoclusters; Chiang et al. 2013). The number (21 peaks) corresponds to number density of $6.4 \times 10^{-8}\,\mathrm{Mpc}^{-3}$ in comoving units. This number density is also comparable to that of known bright radio sources at $z > 2$ (see the section below). However, most of these peaks do not seem to reproduce the high-density contrast seen in the TNJ1338 field. This suggests that high-density regions that host powerful radio galaxies associated with a giant Ly α nebulae, like our observed field, should be much rarer than this.

4.3.2 Density fields around the high-density peaks

Next we checked the density distributions around the 21 density peaks with large Gs found in the simulated map. In order to obtain the density distribution in the same manner as the observed data, we extracted the LAEs within a single Suprime-Cam FoV centred at the peak positions. Then we made the density maps in these fields, and calculated the density distributions using the grid points within the central $40 \times 27.5\,h^{-2}\,\mathrm{Mpc}^2$, similarly to the analyses for the observed LAE sample. Fig. 7 also shows the average density distribution of the fields around the 21 density peaks, together with the errors. This average distribution is shifted towards higher density compared with the whole simulated map, smoothed along the density axis. However, the shape of the distribution does not significantly change: it agrees very closely with that of the whole map if we normalize the density with the average within these 21 fields, instead of the average of the whole simulated map. The distribution again seems to be different from the distribution in the TNJ1338

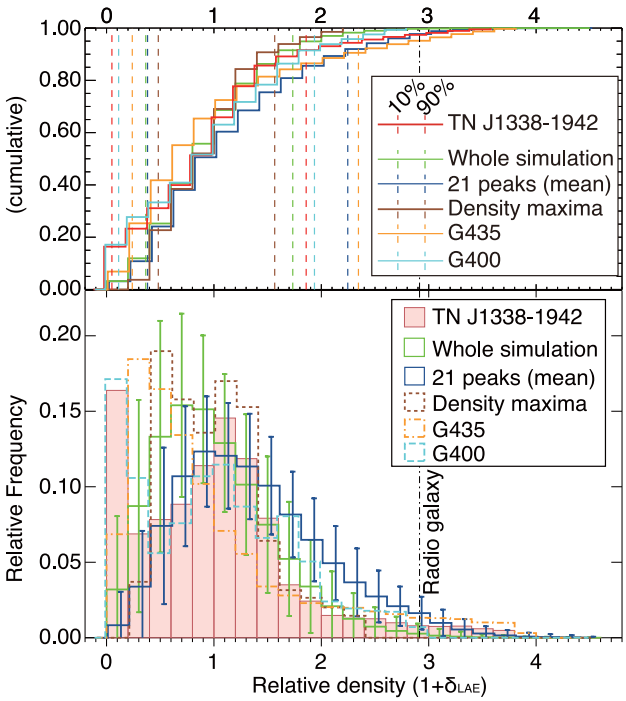

Figure 7. Comparison of the density distributions between the TNJ1338 field and the simulated map with various conditions for the simulation. The filled red histogram shows the observed density distribution of the TNJ1338 field (the same as in Fig. 5 left). The green outlined histogram is the density distribution for the whole simulation volume. The errors were estimated by computing the density distributions for 400 different Suprime-Cam-sized fields centred at random points, calculating the standard deviation for each density bin. The blue outline is the averaged distribution for the 21 fields centred at density peaks higher than the density measured at the radio galaxy position, and with *G*s higher than that of the whole simulated map. The orange dot–dashed and the cyan dashed histograms are for the fields with the largest *G* and the highest void fraction among the 21 fields, respectively (G435 and G400 fields). The brown dotted histogram is for the field around the highest density peak over the whole map. The cumulative distributions are shown in the top panel, together with the 10th and 90th percentiles. The histograms are slightly shifted along the *x*-axis to improve the visibility. The large fractions of pixels in the highest and the lowest density bins cannot be simultaneously reproduced with the simulated density map within the errors. Although the high-density regions can be reproduced at the peak positions, the high volume fraction of the void regions is not seen around typical peaks. The G400 simulated field best reproduces both the large void fraction and the high-density tail seen in the TNJ1338 field. However, the peak of the histogram around the average density ($1 + \delta_{\rm LAE} = 1$) is not so high, and the high-density tail is not so long, compared with those seen in the TNJ1338 field.

field, although the high-density tail is reproduced well. This implies that high-density regions just adjacent to the void regions, like we observed, are still much rarer than simple high-density peaks. For example, we can see that the field around the density maxima (normalized with the average within the same field) shows much narrower distribution than the observed one in the TNJ1338 field.

To further analyse the density distribution, we calculated the Gini coefficient for each map centred at the 21 high-density peaks. Fig. 5 shows the comparison of the Lorentz curves for the observed and simulated density maps. The ordinate corresponds to the cumulative sum of the abscissa of the left-hand panel, normalized with the total sum of the LAE surface density measured at each grid point. This shows that, while the density distribution of the SXDS field is well within the scatter of the simulated map, the distribution of the TNJ1338 field is far from the simulated ones, even from those around most of the density peaks. The possible exceptions are three peaks reproducing the $G \geq 0.4$. These three highest G peaks have $G = 0.435$, 0.403, and 0.400 (hereafter G435, G403, and G400 fields, respectively), which are fairly close to the observed G in the TNJ1338 field. Of these three, two highest G fields (G435 and G403) do not have sufficiently high volume fraction of the void regions, and have only one peak between the average and zero density, as seen in Fig. 7. The G400 field, in contrast, has exceptionally high void fraction (∼15 per cent of the density cells are classified into the lowest density bin). This is the largest void fraction seen in the 94 peaks, which is still ∼1.5 times higher than that in the field with the second largest void fraction (the second largest fraction was found in the G435 field). The G400 field has thus the density distribution closest to that of the TNJ1338 field among the whole simulated map. The peak density of G400 field is $1 + \delta_{\rm LAE} = 3.26$ when normalized with the average over the whole map, and 2.86 when normalized within the same FoV (see Table 4). The other two high-G fields seem to be reproducing better than the G400 field in terms of the peak density, but the density distribution (e.g. the dynamic range and the void fraction) of the G400 field better reproduces the properties of TNJ1338 field.

These results together suggest that the density distribution of the G400 is qualitatively consistent with that of the TNJ1338 field, in terms of the shape of the histogram. The remaining differences might be explained in terms of changes in the galaxy formation processes in such unusually high-density regions harbouring powerful radio galaxies. The simulation does not include Ly α radiation from AGN activity, which can introduce significant differences in the LF, even if the underlying dark matter structure is similar. We then roughly evaluated how well the G400 field reproduces the TNJ1338 field, in terms of the number density: we found no other

Table 4. Statistics of the simulated density field.

Field	Mean[a] (h^2 Mpc^{-2})	Peak[b]	Percentiles[b] 10	50	90	G[c]
G435	0.0409	3.87 (3.17)	0.24 (0.19)	0.71 (0.59)	2.35 (1.92)	0.435
G403	0.0613	2.77 (3.40)	0.24 (0.30)	0.72 (0.89)	2.21 (2.72)	0.403
G400	0.0570	2.86 (3.26)	0.11 (0.13)	0.97 (1.11)	1.94 (2.21)	0.400
Density maxima	0.1104	2.37 (5.24)	0.48 (1.07)	0.97 (2.15)	1.57 (3.46)	0.246
Whole map	0.0499	5.19	0.365	0.92	1.73	0.301

[a]Mean surface density over the field in comoving scale.
[b]In units of the relative density ($1 + \delta_{\rm LAE}$) normalized with the average of the FoV of Suprime-Cam in the same field. Parenthesises show the densities normalized with the average of the whole simulated map.
[c]Gini coefficient of the density distribution.

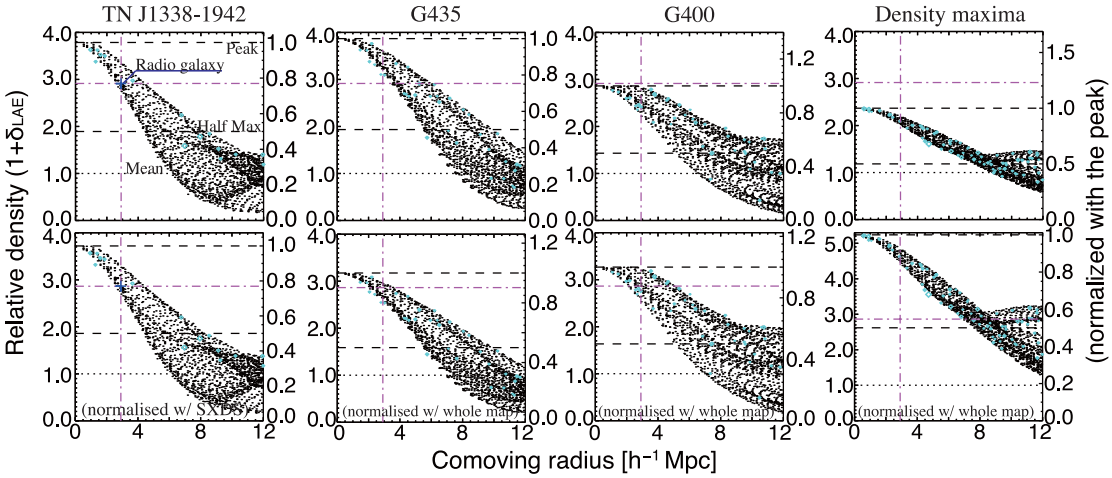

Figure 8. Overdensity profiles around density peaks. Relative overdensity is plotted as a function of the comoving distance from the peak. The leftmost column shows the observed density profile centred at the density peak observed in the TNJ1338 field. The profile in the top panel is based on the density normalized with the average over the FoV of Suprime-Cam in the same field. The density measured at the radio galaxy position is shown with the blue cross. The bottom panel is based on that normalized with the average of the SXDS field. The remaining columns show the profiles of the density peaks found in the simulated map. For each panel, each black point corresponds to the measurement at a single grid point. The LAE positions are marked with cyan diamonds, with the symbol sizes representing the Ly α line luminosities. The mean density is shown by the dotted line, and the peak- and the half-maximum densities are shown by the black dashed lines. The density and the distance measured at the position of the radio galaxy are marked with the magenta dot–dashed lines. The right-hand axis shows the density normalized with the peak value.

G400-like fields within the whole simulation volume of $(500\,h^{-1}\,\mathrm{Mpc})^3$ (comoving). Even the other two high-G fields listed in Table 4 do not reproduce the observed density distribution of the TNJ1338 as good as the G400 field. Since we made four slices with thickness of $112.4\,h^{-1}$ Mpc, this corresponds to a comoving number density of $3.1 \times 10^{-9}\,\mathrm{Mpc}^{-3}$, although the uncertainty is very large because of the small number statistics. This is two orders of magnitude lower than the number density of Virgo-type protoclusters identified in the same Millennium Simulation, and still an order of magnitude lower than Coma-type protoclusters (Chiang et al. 2013). The number density of radio galaxies in the Universe at $2 < z < 5$ is observed to be a few $10^{-8}\,\mathrm{Mpc}^{-3}$ (e.g. Venemans et al. 2007; Miley & De Breuck 2008), comparable to that of the Coma-type protoclusters. This means that the environment of the radio galaxy TNJ1338 is even rarer than the known radio galaxies at $z > 2$. In fact, not all the high-z radio sources have Ly α nebulae extended to $\gtrsim$100 kpc (van Ojik et al. 1997). Such extended Ly α nebulae should reflect exceptionally active interaction between the radio galaxy and its surroundings.

Note again that we found only one field like G400 (or three fields with $G \geq 0.4$) in the whole simulation volume, so the theoretically predicted number density of such high-density region remains significantly uncertain. The observational constraints are also very weak, since there are very few high-z powerful radio galaxies known to date, and the technique finding high-z radio sources, i.e. selecting based on ultrasteep radio spectra, will miss a significant fraction of high-z galaxies (e.g. Ker et al. 2012). Even larger simulations together with more realistic models for LAEs including AGN are needed to calculate accurate statistics for rare density peaks like that in the TNJ1338 field, and to simulate the density field and the LF found around them. In addition, deep and large surveys for high-z radio sources, as well as the follow-up spectroscopy, are needed to more accurately estimate the observed number density of TNJ1338-like regions.

4.3.3 *Density peak profiles*

In order to test how well the simulated map reproduces the observed spatial distribution of the LAE density in the TNJ1338 field, we computed the radial overdensity profile of this peak, and compared with the simulated density map. Fig. 8 shows the comparison of the density profiles between the observed peak in the TNJ1338 field and high-density peaks in the simulated map. The leftmost panels show the observed density profile. As shown in Section 4.1.1, the peak density in the TNJ1338 field is $1 + \delta_{\mathrm{LAE}} = 3.80$, and the radio galaxy position is slightly offset ($\sim 2.8\,h^{-1}$ comoving Mpc) from the peak, at which the density is $\approx$77 per cent of the peak. Although the redshift uncertainty is fairly large, we can roughly estimate the spatial scale wherein the high-density peak is accumulating the material from the surroundings, based on this profile. The radius of half-maximum is $\sim 6\,h^{-1}$ projected comoving Mpc, and the average density within this radius is $1 + \delta_{\mathrm{LAE}} \sim 3$. This could be produced by spherical collapse from a region with radius of $\sim 9\,h^{-1}$ Mpc (comoving). Although this is a very rough estimate, it is clear that the accumulation of material is occurring well within our survey volume. The profile does not significantly change even when normalized with the average density over the SXDS field.

For comparison with this observed density peak profile, we analysed the 94 high-density fields described above (including the three highest G fields). We found that only one of these fields (G435) has peak density as high as the observed one in TNJ1338 field ($1 + \delta_{\mathrm{LAE}} = 3.80$), and 11 fields have the peak density higher than the observed density at the radio galaxy position ($1 + \delta_{\mathrm{LAE}} = 2.91$), when we normalize the density with the average *within* the same Suprime-Cam-sized FoV. When we look into the peak densities normalized with the average over the whole simulated map, 11 have their peak values higher than the observed one in the TNJ1338 field. All except one with $G = 0.356$ have Gs smaller than 0.3. These together suggest that not all the peaks as high as the observed one show high dynamic range within $\sim 50\,h^{-1}$ comoving Mpc scale. To test

how the simulated maps are reproducing such dynamic range, we analysed the radial density profiles of the simulated density peaks. Fig. 8 compares the profiles of three simulated peaks with the observed profile. Table 4 summarizes the statistics of the simulated peaks shown in Fig. 8. The three simulated fields shown here are those with the highest G (G435), the largest void fraction (G400: this field also has the third highest G), and the highest peak density (density maxima when normalized with the whole map) among all the 94 peaks identified above.

The high peak density as we found in the TNJ1338 field is rarely seen in the simulated peaks when normalized within the same FoV. The exceptional cases are only three out of the 94, including the G435 field. The average density of the G435 field is ∼0.8 times the whole map, which is the lowest average density of all the fields centred at the 94 peaks. Although the volume fraction of the void regions is not so large in this field as in the TNJ1338 field, the radial density profile of this peak seems to be reproducing the observed one fairly well. Most of the fields around the 94 peaks, including the G400 field, have their average densities higher than the whole map, in contrast. Even for the G400 field, the average density is higher than the whole simulated map by a factor of ∼1.1. We can see that the peak density is significantly lowered when normalized within the same FoV, although the peak width is comparable to that of the observed peak in the TNJ1338 field. This difference is still much larger in the field around the density maxima. The maximum density exceeds $1 + \delta_{\rm LAE} = 5$ when normalized with the average of the whole map, but goes down to ∼2.4 when normalized within the same FoV. The density contrast in this field is thus fairly small compared with the TNJ1338 field.

Except for the field around the density maxima, wherein the central peak has fairly extended outskirt, the shape of the observed density profile seems to be roughly reproduced by the remaining two simulated peaks selected here. The half-maximum radii are $\sim 6\,h^{-1}$ Mpc, and the peak densities agree with that we observed in the TNJ1338 field within the error (within ±0.5, although it depends on the normalization). The Gini coefficients are also large, $G \geq 0.4$. Comparing the two cases, G435 and G400, the G435 shows better match with the observed profile of the TNJ1338 field in terms of the amplitude and the width of the peak. G400 field also seems to be reproducing the observed profile, but the peak density is only ∼3 when normalized within the same FoV. The shape of the peak seems slightly elongated to form small plateau, leading to the extended component of the peak profile. The peak in the TNJ1338 field seems to be more isolated, while in the G400 field the main peak is facing next to the minor peak with $1 + \delta_{\rm LAE} \sim 2$ leading to the relatively broad outskirt. These results together show that none of the simulated fields simultaneously reproduce the sharp peak profile and the broad density distribution around the peak as we found in the TNJ1338 field.

There are at least three factors which might explain the difficulties in reproducing the density distribution observed in the TNJ1338 field. First, the selection of LAEs in the simulation does not exactly match the observational one. Especially, for the broad-band colours, we did not put any constraints to select the LAEs from the mock catalogue, possibly causing the difference in the selection function. However, this effect is unlikely to significantly change the resulting density distribution. Our mock LAE sample reproduces both the LF and the density distribution of the SXDS control sample quite well. Our selection of LAEs is thus thought to be working well at least for the faint end of the LF, where the TNJ1338 and the mock samples agree with each other. The second possibility is that the LAE model itself is not sufficiently realistic. For example, the escape fraction of Ly α photons is assumed to be constant for all the LAEs. If the escape fraction is changed in highly overdense regions by e.g. galaxy–galaxy interactions or AGN feedback, the spatial distribution of LAEs may significantly change in the field. This is also related to the third factor, i.e. the observations might include a significant contribution of Ly α coming from AGN, which is not included in the model. AGN activity may affect the galaxy formation processes of the surroundings through, e.g. induced star formation (Zirm et al. 2005). Such AGN activity may be enhanced in overdense environments (e.g. Pentericci et al. 2002; Croft et al. 2005; Lehmer et al. 2009; Digby-North et al. 2010). If the bright LAEs in our TNJ1338 sample are predominantly AGNs, this could lead to significant enhancement of the LAE number density, emphasizing the density contrast.

Another, much more naive interpretation is that the Millennium Simulation is not large enough to reproduce this kind of overdensity. This is in case if the halo mass of the overdensity is significantly larger than the maximum halo mass of the Millennium Simulation. Even if the SXDS field is suffering from overdensities and our density normalization is not correct, such a steep and high-density peak with large density contrast, as well as the shape of the density histogram, is not reproduced in the current simulation. The disagreement may be overcome by carrying out even larger simulations. The density profiles around massive haloes in such a large simulation may be different from those around less massive haloes: extremely massive haloes possibly form very high density peaks without significant growth in size of the overdense regions.

The observational uncertainties may also affect the density distribution. Since we do not have accurate redshifts for most of our LAEs, our estimates of the Ly α luminosity have large uncertainty. This may especially affect the completeness for the faint sources, and our detection completeness at faint end may be lower than expected. The density distribution of the mock LAEs is dominated by relatively faint LAEs, so that some fraction of faint LAEs might be missed in our observed data, resulting in apparently high peak density and density contrast. Indeed, when we use 30 brightest LAEs within each field of the simulation to compute the density map, instead of normalizing the density, the density distribution for some fields in the simulation becomes closer to the observed one in the TNJ1338 field. However, even for the field giving the best match with the observed density distribution in this case, such a steep, isolated density peak cannot be reproduced. We still need fine tuning to reproduce the simulated density field with observed one.

In any case, more precise measurement of the density field and constraints on the AGN activity in our LAEs are needed to test the possibilities described here.

4.3.4 *Luminosity function*

Fig. 6 also shows the LF of the mock LAE sample. Again this sample is selected with the same colour constraints as the TNJ1338 sample. The mock catalogue has been already shown to have a Ly α LF reproducing well that of O08's sample (Orsi et al. 2008). This means that the mock sample is expected to reproduce the LF of our control sample. The LF of the mock sample agrees quite well with the control sample, although except for the bright end ($\log L_{{\rm Ly}\alpha} \sim 43.6$). This difference is thought to come from the cosmic variance. The bright end of the LF of our control sample is determined with a single source, and the probability of detecting such bright sources within a single FoV is relatively low. Even for the fields around the high-density peaks with large Gs selected

above, 10 out of the 21 fields do not contain any sources with $\log L_{\mathrm{Ly}\alpha} \sim 43.6$ (the remaining 11 fields contain only one such bright source each).

Similarly to the comparison with the blank fields, the LF in the whole TNJ1338 field is higher than the mock LAE LF at the bright end, but the difference is much larger than the case of the control sample. The LF of the whole TNJ1338 field is factor of ∼10 higher than the mock LF at the bright end, $\log L_{\mathrm{Ly}\alpha} \sim 43.6$. The difference becomes a factor of ∼20 when we look into the LF of the overdense regions of TNJ1338 field. For the fainter range, the TNJ1338 LF comes below that of mock LAEs at $\log L_{\mathrm{Ly}\alpha} \sim 43.0$. The crossing point is in between these two, i.e. the number of LAEs fainter than $\log L_{\mathrm{Ly}\alpha} \sim 43.0$–43.3 seems to be relatively suppressed in this field. The faint end of the LF agrees with the mock, when we look at the LF of the overdense regions in the TNJ1338 field. While the faint-end LF of this field does not show any enhancement compared to the mock LF, the bright end shows a large enhancement by one order of magnitude. This again suggests that the TNJ1338 field is a peculiar field dominated by bright LAEs, or AGN hosts including the host of the radio galaxy. There are four bright LAEs contained in the two highest luminosity bins ($\log L_{\mathrm{Ly}\alpha} \sim 43.6$ and 43.9) in this field, and such bright sources are likely to be hosting AGN, as suggested by O08. Such a population of bright LAEs, as well as the unusually high galaxy overdensity, should largely affect the galaxy formation within this field.

The main differences between the TNJ1338 and the mock LAE samples in terms of LFs are then thought to be (1) the presence of the AGN, (2) the high-density peak as high as $1 + \delta_{\mathrm{LAE}} \sim 4.1$, and (3) the large density contrast within a single FoV of the Suprime-Cam. Of these three, (2) can be partly reproduced with the mock sample as described in Sections 4.3.1 and 4.3.3. We then tested how the LF differs from the observed one when one of these three main discrepancies are partly solved, by computing the LF within the peak regions seen in the simulated map. The resulting LFs in overdense regions show almost the same shape as the LF from the whole mock sample, and the amplitude of the LF becomes higher by up to 0.4 dex. We can see in Fig. 6 that only ∼50 per cent (11 fields) of the 21 high-density fields contain LAEs with $\log L_{\mathrm{Ly}\alpha} \sim 43.6$. Although most of these 11 fields contain only one source each, we can estimate the bright end of the LF by averaging the 21 fields, $\log n_{\mathrm{LAE}} = -5.56$ at the bright end. This value is only 0.08 dex higher value than the total mock sample. This means that there are no significant enhancements of the number (fraction) of bright LAEs such as we found in the TNJ1338 field. While the enhancements of the total number density of LAEs are relatively well reproduced in these high-density fields, the LF shape remains almost unchanged from that of the whole mock sample, i.e. not biased to bright sources.

Note that not all of the high-density peaks described in Section 4.3.3 are included in the 11 fields containing such brightest LAEs: the field around density maxima contains only one, and G435, G403, and G400 fields contain no such LAEs as bright as $\log (L_{\mathrm{Ly}\alpha}) \sim 43.6$. This simply means that the brightest LAEs are likely to be found in fields with high average density, but not necessarily with high-density contrast. This is also expected from the properties of the mock LAEs: the galaxy bias positively correlates with the Ly α luminosity $L_{\mathrm{Ly}\alpha}$, but changes by only a factor of ∼2–3 (Le Delliou et al. 2006; Orsi et al. 2008). On the other hand, the LFs of our *observed* samples suggest that the bias depends more strongly on $L_{\mathrm{Ly}\alpha}$. The mock LAE sample does not contain AGN at all, so that it can reproduce only the properties of 'normal' LAEs, not LAEs hosting AGNs, nor AGN-induced star formation. Activity related to such AGN, e.g. AGN-induced star formation in the vicinity of the radio galaxy (Zirm et al. 2005), may lead to enhancements of star formation in this high-density region. Such interactions between the AGN and the surrounding environment may also occur further out from the central radio galaxy, as the extended Ly α nebula is observed up to ∼100 kpc (Venemans et al. 2002). For some Ly α nebulae, interaction is (although indirectly) suggested even further out from their alignment with the surrounding large-scale structure up to $\sim 10\,h^{-1}$ comoving Mpc (Erb et al. 2011). Furthermore, three out of the four LAEs mentioned above in the highest luminosity bins in the TNJ1338 sample, as well as the radio galaxy, lie within the overdense ($1 + \delta_{\mathrm{LAE}} > 1$) regions. These may together suggest that star formation/AGN activity is enhanced by the presence of AGN in the overdense regions, while there are no such sources of enhancement in the underdense regions.

Such an enhancement is expected from the high galaxy density, leading to frequent galaxy mergers. The high density may also lead to high gas accretion rates, which enhances the star formation/AGN activity resulting in bright LAEs. These mechanisms will result in a large bias of the bright LAEs, dominating the bright end of the LF. Such a large bias for bright LAEs results in the large density contrast of bright LAEs described in Section 4.1.2. In order to see how such an enhancement affects the LF of *normal* star-forming galaxies in the overdense environment, we need to take deeper images to construct a sample of much fainter LAEs. We still have difficulties to make a meaningful comparison with the simulation, due to the shallowness of the data: the luminosity range of our observed samples corresponds to the very bright end of the mock LAEs. Constructing a sample of fainter LAEs (down to $\log (L_{\mathrm{Ly}\alpha}) \sim 42.7$ or fainter), which is less likely to be contaminated by AGN, is essential to probe the LF and its environmental dependence. The uncertainty in the redshifts is also a problem in computing the galaxy density and the luminosities, as well as evaluating the contamination of AGN and foreground galaxies. Further deep imaging to construct a deeper sample, and subsequent follow-up spectroscopy, are needed to draw further information from this comparison.

5 CONCLUSIONS

We have carried out intermediate-band and broad-band imaging observations with Suprime-Cam on the *Subaru* Telescope of a $z = 4.1$ radio galaxy associated with a giant Ly α nebula to probe its environment on a $\sim 50\,h^{-1}$ Mpc scale. In order to quantify the environment with a control sample, we utilized the existing data from a blank field, SXDS, taken with the same instrument and similar filters. We also used a mock LAE catalogue generated with a semi-analytical galaxy formation model based on the Millennium Simulation.

We confirmed that the radio galaxy lies in a region with peak LAE number density of $1 + \delta_{\mathrm{LAE}} = 3.8 \pm 0.5$ at the radio galaxy position, even after taking account of the relatively large redshift range covered by the *IA624* filter. The average density over the Suprime-Cam FoV is almost the same as that of the blank field within 2 per cent, showing that the density contrast in this field is very high. These results suggest that radio galaxies associated with Ly α nebulae emerge in extreme overdensity environments. Comparing these with the mock LAEs, we found that such high-density regions are quite rare, 27 peaks in the whole simulation volume of $(500\,h^{-1}\,\mathrm{Mpc})^3$, and correspond to the densest <0.4 percentile. The corresponding number density is comparable to that of Coma-type protoclusters found in the same simulation, and known radio galaxies at $z > 2$. The overdensity associated with the radio galaxy can be traced up to ∼3–6 comoving Mpc, facing the large void region just adjacent to it. Only one of the 35 density

peaks have such a large density contrast on this scale, and even this peak cannot fully reproduce the density peak profile.

We found the density dependence of the LFs. The Ly α LF of the TNJ1338 field shows enhancement at the bright end ($\log(L_{\mathrm{Ly}\alpha}[\,\mathrm{erg\,s^{-1}}]) \gtrsim 43.3$) by an order of magnitude or more, while the faint end almost agrees with that in the blank field. We compared the LFs with the mock LAEs to conclude that star formation and/or AGN activities affecting the bright end of the LF are highly enhanced within overdense regions. We pointed out the possibilities that frequent galaxy mergers or high gas accretion rate enhance the star formation/AGN activity, or AGN-induced star formation in this field. The presence of a powerful radio galaxy showing a giant Ly α nebula is thus a possible signpost of changes in galaxy formation activity on scales of $\sim$3–6 comoving Mpc.

ACKNOWLEDGEMENTS

We acknowledge the anonymous referee, who gave us important and practically useful comments to improve the draft. We thank Masami Ouchi for providing the data of luminosity functions, and giving us useful comments. We thank Yi-Kuan Chiang, Roderik Overzier, Surhud More, John Silverman, Masao Mori, and Takatoshi Shibuya for having discussion over this work, and giving us valuable comments. This work was supported by the FIRST programme 'Subaru Measurements of Images and Redshifts (SuMIRe)', World Premier International Research Center Initiative (WPI Initiative), MEXT, Japan. This work was supported in part by the Science and Technology Facilities Council rolling grant ST/I001166/1 to the ICC. Calculations were partly performed on the ICC Cosmology Machine, which is part of the DiRAC Facility jointly funded by STFC and Durham University. YM acknowledges support from JSPS KAKENHI grant number 20647268. IS acknowledges support from STFC (ST/I001573/1), the ERC Advanced Investigator programme DUSTYGAL 321334 and a Royal Society/Wolfson Merit Award. The data were in part obtained from SMOKA, which is operated by the Astronomy Data Center, National Astronomical Observatory of Japan.

REFERENCES

Atek H. et al., 2011, ApJ, 743, 121
Baba H. et al., 2002, in Bohlender D. A., Durand D., Handley T. H., eds, ASP Conf. Ser. Vol. 281, Astronomical Data Analysis Software and Systems XI. Astron. Soc. Pac., San Francisco, p. 298
Basu-Zych A., Scharf C., 2004, ApJ, 615, L88
Bertin E., Arnouts S., 1996, A&AS, 117, 303
Blain A. W., Chapman S. C., Smail I., Ivison R., 2004, ApJ, 611, 725
Bruzual G., Charlot S., 2003, MNRAS, 344, 1000
Capak P. L. et al., 2011, Nature, 470, 233
Chambers K. C., Miley G. K., van Breugel W. J. M., 1990, ApJ, 363, 21
Chiang Y.-K., Overzier R., Gebhardt K., 2013, ApJ, 779, 127
Colbert J. W., Scarlata C., Teplitz H., Francis P., Palunas P., Williger G. M., Woodgate B., 2011, ApJ, 728, 59
Cole S., Lacey C. G., Baugh C. M., Frenk C. S., 2000, MNRAS, 391, 168
Croft S., Kurk J., van Breugel W., Stanford S. A., de Vries W., Pentericci L., Röttgering H., 2005, AJ, 130, 867
Dawson S. et al., 2004, ApJ, 617, 707
Dawson S., Rhoads J. E., Malhotra S., Stern D., Wang J.-X., Dey A., Spinrad H., Jannuzi B. T., 2007, ApJ, 671, 1227
De Breuck C., van Breugel W., Minniti T., Miley G. K., Röttgering H. J. A., Stanford S. A., Carilli C., 1999, A&A, 352, L51
De Breuck C. et al., 2001, ApJ, 121, 1241
De Breuck C. et al., 2004, A&A, 424, 1
Dekel A. et al., 2009, Nature, 457, 451
Digby-North J. A. et al., 2010, MNRAS, 407, 853
Dijkstra M., Kramer R., 2012, MNRAS, 424, 1672
Dijkstra M., Loeb A., 2009, MNRAS, 408, 1109
Dijkstra M., Haiman Z., Spaans M., 2006, ApJ, 649, 14
Erb D. K., Bogosavljević M., Steidel C. C., 2011, ApJ, 740, L31
Fardal M. A., Katz N., Gardner J. P., Hernquist L., Weinberg D. G., Davé R., 2001, ApJ, 562, 605
Faucher-Giguére C.-A., Kereš D., Dijkstra M., Hernquist L., Zaldarriaga M., 2010, ApJ, 725, 633
Fukugita M., Shimasaku K., Ichikawa T., 1995, PASP, 107, 945
Furlanetto S. R., Schaye J., Springel V., Hernquist L., 2005, ApJ, 622, 7
Furusawa H. et al., 2006, ApJS, 176, 1
Geach J. E. et al., 2005, MNRAS, 363, 1398
Geach J. E. et al., 2009, ApJ, 700, 1
Goerdt T., Dekel A., Sternberg A., Ceverino D., Teyssier R., Primack J. R., 2010, MNRAS, 407, 613
Hayashino T. et al., 2000, Proc. SPIE, 4008, 397
Intema H. T., Venemans B. P., Kurk J. D., Ouchi M., Kodama T., Röttgering H. J. A., Miley G. K., Overzier R. A., 2006, A&A, 456, 433
Ivison R. J. et al., 2013, ApJ, 772, 137
Iye M. et al., 2004, PASJ, 56, 381
Kakazu Y., Cowie L., Hu E., 2007, ApJ, 668, 853
Kennicut R. C., 1983, MNRAS, 301, 569
Ker L. M., Best P. N., Rigby E. E., Röttgering H. J. A., Gendre M. A., 2012, MNRAS, 420, 2644
Kereš D., Katz N., Weinberg D. H., Davé R., 2005, MNRAS, 363, 2
Kovač K., Somerville R. S., Rhoads J. E., Malhotra S., Wang J.-X., 2007, ApJ, 668, 15
Koyama Y. et al., 2013, MNRAS, 434, 423
Le Delliou M., Lacey C., Baugh C. M., Guiderdoni B., Bacon R., Courtois H., Sousbie T., Morris S. L., 2005, MNRAS, 357, L11
Le Delliou M., Lacey C., Baugh C. M., Morris S. L, 2006, MNRAS, 365, L712
Lehmer B. D. et al., 2009, MNRAS, 400, 299
Madau P., 1995, ApJ, 441, 18
Massey P., Strobel K., Barnes J. V., Anderson E., 1988, ApJ, 328, 315
Matsuda Y., Yamada T., Hayashino T., Yamauchi R., Nakamura Y., 2006, ApJ, 640, L123
Matsuda Y. et al., 2011, MNRAS, 410, L13
Matsuda Y. et al., 2012, MNRAS, 425, 878
Miley G., De Breuck C., 2008, ARA&A, 15, 67
Miley G. et al., 2004, Nature, 427, 47
Miyazaki S. et al., 2002, PASJ, 54, 833
Mori M., Umemura M., 2006, Nature, 440, 644
Nilsson K. K., Fynbo J. P. U., Møller P., Sommer-Larsen J., Ledoux C., 2006, A&A, 452, L23
Ohyama Y. et al., 2003, ApJ, 591, L9
Oke J. B., 1974, ApJS, 27, 21
Orsi A., lacey C., Baugh C. M., Infante L., 2008, MNRAS, 391, 1589
Ouchi M. et al., 2004, ApJ, 611, 660
Ouchi M. et al., 2005, ApJ, 620, L1
Ouchi M. et al., 2008, ApJS, 176, 301 (O08)
Ouchi M. et al., 2010, ApJ, 723, 869
Overzier R. A. et al., 2008, ApJ, 673, 143
Overzier R. A., Nesvadba N. P. H., Dijkstra M., Hatch N. A., Lehnert M. D., Villar-Martiniń M., Wilman R. J., Zirm A. W., 2013, ApJ, 771, 89
Pentericci L., Kurk J. D., Carilli C. L., Harris D. E., Miley G. K., Röttgering H. J. A., 2002, A&A, 396, 109
Rees M. J., Ostriker J. P., 1977, MNRAS, 179, 541
Reuland M. et al., 2003, ApJ, 592, 755
Rhoads J. E., Malhotra S., Dey A., Stern D., Spinrad H., Jannuzi B. T., 2000, ApJ, 545, L85
Röttgering H. J. A., Hunstead R., Miley G. K., van Ojik R., Wieringa M. H., 1995, MNRAS, 277, 389
Saito T., Shimasaku K., Okamura S., Ouchi M., Akiyama M., Yoshida M., 2006, ApJ, 648, 54

Saito T., Shimasaku K., Okamura S., Ouchi M., Akiyama M., Yoshida M. Ueda Y., 2008, ApJ, 675, 1076
Schlegel D. J., Finkbeiner D. P., Davis M., 1998, ApJ, 500, 525
Smail I., Blundell M., 2013, MNRAS, 434, 3246
Smith D. J. B., Jarvis M. J., 2007, MNRAS, 378, L49
Springel V. et al., 2005, Nature, 435, 629
Steidel C. C., Adelberger K. L., Shapley A. E., Erb D. K., Reddy N. A., Pettini M., 2005, ApJ, 626, 44
Steidel C. C., Erb D. K., Shapley A. E., Pettini M., Reddy N., Bogosalević M., Rudie G. C., Rakic O., 2010, ApJ, 717, 289
Stone R. P. S., 1996, ApJS, 107, 423
Taniguchi Y., 2004, in Arimoto N., Duschi W., eds, Studies of Galaxies in the Young Universe with New Generation Telescope, p. 107, preprint (arXiv:astro-ph/0301097)
Taniguchi Y., Shioya Y., 2000, ApJ, 532, L13
Tenorio-Tagle G., Silich S. A., Kunth D., Terlevich E., Terlevich R., 1999, MNRAS, 309, 332
Uchimoto Y. K. et al., 2008, PASJ, 60, 683
Uchimoto Y. K. et al., 2012, ApJ, 750, 116
van der Wel A. et al., 2011, ApJ, 742, 111
van Ojik R., Röttgering H. J. A., Carilli C., Bremer M. N., Macchetto F. A., 1996, A&A, 313, 25
van Ojik R., Röttgering H. J. A., Miley G. K., Hunstead R. W., 1997, A&A, 317, 358
Veilleux S., Cecil G., Bland-Hawthorn J., 2005, ARA&A, 43, 769
Venemans B. et al., 2002, ApJ, 569, L11
Venemans B. et al., 2007, A&A, 461, 823
Villar-Martin M., Sánchez S. F., Humphrey A., Dijkstra M., di Serego Alighieri S., De Breuck C., Gonzalez Delgado R., 2007, MNRAS, 378, 416
Wilman R. J., Gerssen J., Bower R. G., Morris S. L., Bacon R., de Zeeuw P. T., Davies R. L., 2005, Nature, 436, 227
Yagi M., Kashikawa N., Sekiguchi M., Doi M., Yasuda N., Shimasaku K., Okamura S., 2002, AJ, 123, 66
Zirm A. W. et al., 2005, ApJ, 630, 68

APPENDIX A: THREE-DIMENSIONAL DENSITY PROFILES

As discussed in Section 4.3.2, such a high-density peak and a large void region within a single FoV as we found in the TNJ1338 field is likely to be reproduced by fields with large *G*s, like the G435 or G400 field. However, although the G435 field has very large *G* the volume fraction of the void regions is not as high as that in the TNJ1338 field, the shape of the peak profile is relatively well reproduced. The G400 field reproduces the observed large void fraction, the shape of the density histogram, and the small difference between the two cases of normalization, but does not reproduce the peak profile well compared with the G435 field. Unlike these high-*G* fields, the field around the density maxima has rather different peak profile and density distribution, although the peak density is the highest when normalized with the whole map.

In addition to such statistics of the two-dimensional density distribution, the three-dimensional (3D) density gives useful information to infer how well the simulation reproduces the observed density field, as well as to infer the underlying 3D structure of the TNJ1338 field. We calculated the local and global densities using the 3D spatial distribution of the mock LAEs within these fields. The density at the position of each source was calculated based on the distance to the 5th-, 10th- and 20th-nearest neighbour. We normalized the density with the average number density over the same field, and calculated the overdensity $\delta_{5\mathrm{th}}$, $\delta_{10\mathrm{th}}$, and $\delta_{20\mathrm{th}}$. Then we counted the LAEs residing in the density greater than the average. Table A1 summarizes the results of the density measurements of these three high-density fields, comparing with the observed data.

Comparing the three high-*G* fields and the field around the density maxima, we cannot see significant differences in the fraction of LAEs lying within the overdensities in terms of $\delta_{5\mathrm{th}}$. On the other hand, the fraction of LAEs lying within the $\delta_{20\mathrm{th}} > 0$ is much higher around the density maxima than in the other three high-*G* fields (∼20 per cent for the maxima and <2 per cent for the three high-*G* fields). This means that the clustering signal of LAEs is comparable for all the four high-density fields in ∼14–17 h^{-1} Mpc scale, but much stronger around the density maxima in ∼22 h^{-1} Mpc scale (both in comoving units). The overdensity (i.e. protocluster) associated with the density maxima is thus thought to be more evolved compared with other three high-*G* fields, resulting in such a large size filling a large fraction of our FoV to have relatively low *G*. Fig. A1 clearly shows such trend. For high-*G* fields, size of each overdense clump is relatively small, and the fraction of void regions is higher than in the density maxima. The surface density peak in the G435 field seems to be dominated by a single density peak at $z \sim 460$, but we can see at least three peaks along the z-axis in the G400 field (the G403 field similarly has three or more peaks nearly along the z-axis, although not shown in Fig. A1).

As seen in Fig. A1, most of the high-density peaks are likely to be elongated structures or two or more small high-density clumps aligned with the line of sight, rather than single extremely

Table A1. Density measurements around the high-density peaks.

Field	N_{tot}[a]	max$(1+\delta_{\mathrm{LAE}})$[b]	$N(\delta_{\mathrm{LAE}}>0)$[c]	$N(\delta_{5\mathrm{th}}>0)$[d]	$N(\delta_{10\mathrm{th}}>0)$[d]	$N(\delta_{20\mathrm{th}}>0)$[d]
G435	66	3.9	39 (34)	16	10	1
G403	112	2.8	74 (84)	38	27	2
G400	92	2.9	69 (73)	27	6	0
Density maxima	192	2.4	121 (174)	74	53	43
TN J1338−1942	30[e]	3.8	26[e]	–	–	–
(SXDS)[f]	34	2.4	29	–	–	–

[a]Total number of LAEs within the field.
[b]The peak (maximum) surface density within the field.
[c]The number of LAEs with the surface density greater than the average. The numbers in parenthesises are based on the average over the whole map.
[d]The number of LAEs with the 3D densities greater than the average over the whole simulation volume. The densities were calculated from the 5th-, 10th- and 20th-nearest neighbours for $\delta_{5\mathrm{th}}$, $\delta_{10\mathrm{th}}$ and $\delta_{20\mathrm{th}}$, respectively.
[e]The radio galaxy is not counted.
[f]Control field (not a high-density peak).

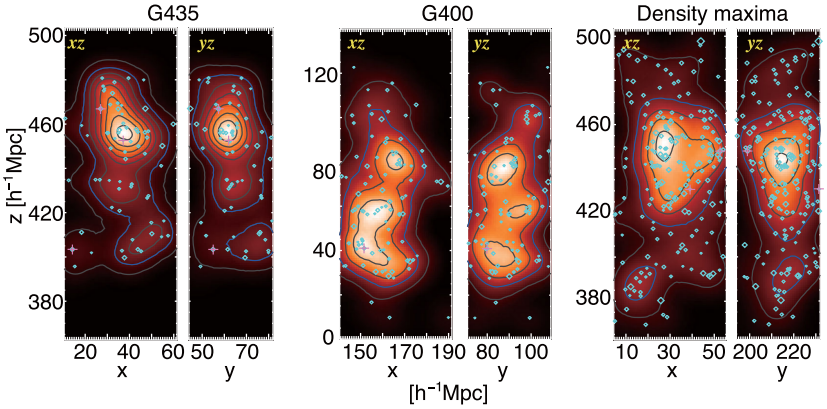

Figure A1. LAE density maps of the three fields with high-density peaks, generated with the mock LAEs projected on to the *xz* and *yz* planes, instead of the *xy* plane shown in Fig. 4. The leftmost two panels are the maps for the G435 field, projected on the *xz* (left) and the *yz* plane (right). The two panels on the centre are for the G400 field, and the rightmost two panels are for the field centred at the density maxima. All the coordinates shown here are in the comoving scales. The maps are drawn with the same manner as in Fig. 4, except for the use of smoothing radius of $8\,h^{-1}$ Mpc. The density shown here is normalized with the average over the same field. LAEs associated with the largest halo mass over each field are marked with the magenta crosses. For all the three peaks shown here, there seems to be elongated filamentary structure nearly along the *z*-axis. This is quite common in the 94 high-density peaks we found in the simulated density map. The overdense region in the G435 field emerged on the *xy*-plane density seems to be dominated by a single high-density peak at $z \sim 460$. This peak is relatively compact compared with that seen in the density maxima around $z \sim 440$. For the G400 field, in contrast, there are at least three compact high-density clumps nearly along the *z*-axis. Such alignment of subclimps can be seen in most of the 21 high-*G* peaks we found in the simulated map.

overdense regions. If radio galaxies are formed within single extremely overdense regions, the high-density region seen around the density maxima is more likely to be reproducing the environment of the radio galaxy. However, as expected from the lower *G* compared with the observed one in the TNJ1338 field, the field around the density maxima does not have such a large fraction of void regions. The G400 field, which has an exceptionally large void fraction, has at least three subclumps along the filamentary structure. Since this is quite common feature in high-density fields (or in high-*G* fields), the overdensity found in the TNJ1338 field might be the result of such alignment of more than two subclumps. The observed overdensity around the radio galaxy might be dominated by a single extremely overdense clump as well, as the G435 field reproduces the observed density profile better than the G400 field (see Fig. 8).

We also analysed the relation between the 3D density distribution and the maximum dark halo mass hosting the LAEs in the fields around the 94 peaks. We found five peaks containing a dark halo with the maximum mass in the simulation, $9.4 \times 10^{12}\,M_{\odot}$. These five peaks all have relatively low Gini coefficients, $G \leq 0.27$, and none of the four peaks listed in Table A1 are included in these five. The most massive haloes found in the four peaks in Table A1 have the mass of $2.4 \times 10^{12}\,M_{\odot}$, which are contained in the G400 and G403 fields. These massive haloes are apparently associated with the highest density peak of each field. The maximum halo mass found in the remaining two fields are $8.3 \times 10^{11}\,M_{\odot}$ and $1.7 \times 10^{12}\,M_{\odot}$ for the G435 and the density maxima, respectively. For the G435 field one of the most massive dark halo can be seen very close to the highest density peak, while for the density maxima such massive haloes can be seen only at the outskirts of the peak. There seems to be no significant correlations between the maximum halo mass of the field and the density peak profiles. On the other hand, the peak of the density maxima does not have the most massive dark haloes around its centre, while the three high-*G* fields all have the most massive haloes close to the centres of their highest peaks. This difference might be reflecting how the overdensities have accreted their mass until the observed epoch.

These analyses together suggest that the simulation cannot fully reproduce the density distribution of the TNJ1338 field. It is likely that more than two (relatively compact) high-density clumps are well aligned with the line of sight, at least one of which have the most massive dark haloes of the system near the centres. In any case, further detailed analyses with more realistic models of galaxy formation are needed to draw definite conclusions on the true 3D distribution of LAEs and the mass accretion mechanisms of the protocluster.

[1]*Institute for Cosmic Ray Research, The University of Tokyo, 5-1-5 Kashiwanoha, Kashiwa, Chiba 277-8583, Japan*
[2]*Kavli Institute for the Physics and Mathematics of the Universe (WPI), Todai Institutes for Advanced Studies, The University of Tokyo, 5-1-5 Kashiwanoha, Kashiwa, Chiba 277-8583, Japan*
[3]*National Astronomical Observatory of Japan, 2-21-1 Osawa, Mitaka, Tokyo 181-8588, Japan*
[4]*The Graduate University for Advanced Studies (SOKENDAI), 2-21-1 Osawa, Mitaka, Tokyo 181-0015, Japan*
[5]*Institute for Computational Cosmology, Department of Physics, Durham University, South Road, Durham DH1 3LE, UK*
[6]*Instituto de Astrofisica, Facultad de Fisica, Pontificia Universidad Católica, Av. Vicuña Mackenna 4860, Santiago, Chile*
[7]*Centro de Astro-Ingenieria, Pontificia Universidad Católica, Av. Vicuña Mackenna 4860, Santiago, Chile*
[8]*College of General Education, Osaka Sangyo University, 3-1-1, Nakagaito, Daito, Osaka 574-8530, Japan*
[9]*Subaru Telescope, National Astronomical Observatory of Japan, 650 North A'ohoku Place, Hilo, HI 96720, USA*
[10]*Astronomical Institute, Tohoku University, Aramaki, Aoba, Sendai 980-8578, Japan*
[11]*Department of Astronomy, Kyoto University, Kyoto 606-8502, Japan*
[12]*European Southern Observatory, Karl Schwarzschild Straße 2, D-85748 Garching, Germany*
[13]*Research Center for the Space and Cosmic Evolution, Ehime University, 2-5 Bunkyo-cho, Matsuyama, Ehime 790-8577, Japan*

This paper has been typeset from a TEX/LATEX file prepared by the author.